`DeST-OT`: Alignment of Spatiotemporal Transcriptomics Data

Peter Halmos[*1], Xinhao Liu[*1], Julian Gold[2], Feng Chen[3], Li Ding[3,4], and Benjamin J. Raphael[†1]

[1]Department of Computer Science, Princeton University, 35 Olden St, Princeton, NJ 08544
[2]Center for Statistics and Machine Learning, Princeton University, 26 Prospect Ave, Princeton, NJ 08544
[3]Departments of Medicine and Genetics, Siteman Cancer Center, Washington University in St. Louis, St. Louis, MO 63110
[4]McDonnell Genome Institute, Washington University in St. Louis, St. Louis, MO 63108

Abstract

Spatially resolved transcriptomics (SRT) measures mRNA transcripts at thousands of locations within a tissue slice, revealing spatial variations in gene expression and distribution of cell types. In recent studies, SRT has been applied to tissue slices from multiple timepoints during the development of an organism. Alignment of this *spatiotemporal* transcriptomics data can provide insights into the gene expression programs governing the growth and differentiation of cells over space and time. We introduce `DeST-OT` (**De**velopmental **S**patio**T**emporal **O**ptimal **T**ransport), a method to align SRT slices from pairs of developmental timepoints using the framework of optimal transport (OT). `DeST-OT` uses *semi-relaxed* optimal transport to precisely model cellular growth, death, and differentiation processes that are not well-modeled by existing alignment methods. We demonstrate the advantage of `DeST-OT` on simulated slices. We further introduce two metrics to quantify the plausibility of a spatiotemporal alignment: a *growth distortion metric* which quantifies the discrepancy between the inferred and the true cell type growth rates, and a *migration metric* which quantifies the distance traveled between ancestor and descendant cells. `DeST-OT` outperforms existing methods on these metrics in the alignment of spatiotemporal transcriptomics data from the development of axolotl brain.

Code availability: Software is available at `https://github.com/raphael-group/DeST_OT`

---

[*]These authors contributed equally to this work, and the order is decided by a coin flip.
[†]Correspondence: `braphael@princeton.edu`

1   Introduction

Spatially Resolved Transcriptomics (SRT) technologies [37, 33, 28] measure gene expression simultaneously from thousands of cells or spots from a tissue slice, linking the gene expression measurement to the physical location within the tissue. These technologies enable exploration of tissue organization by analyzing cells within their native microenvironment, opening the door to the study of spatial biology [1, 17]. In some cases, SRT is applied to multiple slices from the same tissue. Joint analysis of multi-slice spatial data helps with the data sparsity problem in individual slices, enabling downstream analyses such as 3D differential expression or 3D cell-cell communication [23]. Multiple methods have been developed for alignment of multi-slice SRT data. For example, PASTE [45] integrates multiple slices from the same tissue and reconstructs the tissue gene expression in 3D, and PASTE2 [24] extends PASTE to partially overlapping slices. STalign [8] is an image registration method finding a diffeomorphism between the H&E images of two spatial slices. GPSA [18] uses Gaussian processes to register spatial slices onto a common coordinate system, while SLAT [44] relies on graph neural networks and adversarial learning.

Another recent exciting application is to apply SRT to tissues taken from multiple timepoints of a developmental process [5]. Alignment of slices from multiple timepoints can provide insights into the gene expression programs governing the growth and differentiation of cells over space and time. However, alignment of spatiotemporal transcriptomics data presents unique challenges as there is a complicated interplay between proliferation and apoptotic cell dynamics in the sculpting of developing tissue [42]. Regions of the tissue may grow or shrink, creating many-to-one relationships between the spots from consecutive timepoints. Cells also change in gene expression and differentiate into new cell types during development. Moreover, slices no longer come from the same batch (individual or time-point) and thus may exhibit batch effects.

The existing methods for temporal alignment of single-cell data or for spatiotemporal alignment suffer from important limitations. Waddington-OT [34] aligns temporal single cell data for reprogramming datasets, but does not take spatial information into account. A recent preprint [21] describes moscot, a method that relaxes the OT formulation in PASTE to use *unbalanced optimal transport* [36]. moscot allows for cell growth and death using a curated set of proliferation and apoptosis genes as prior knowledge but optimizes an objective function that encourages static shape-matching. Other works [18, 44] do not necessarily quantify growth, and often have methodological and robustness limitations.

We introduce DeST-OT, a method to align spatiotemporal transcriptomics data that consists of SRT slices from multiple timepoints. DeST-OT proposes a novel *semi-relaxed* optimal transport framework, leading to unsupervised discovery of cell growth and apoptosis without relying on existing gene annotations. DeST-OT aligns differentiating cells along a manifold jointly defined by transcriptomic information and spatial information, leading to both biologically and physically valid alignments. DeST-OT accounts for spatiotemporal scenarios by modeling three orders of interactions between cells in a developing tissue, bridging a gap in the standard Fused Gromov-Wasserstein (FGW) OT objective [38].

We demonstrate the advantages of DeST-OT on both simulated spatiotemporal data and spatiotemporal data from axolotl brain development. To evaluate the performance of different methods we introduce the *growth distortion metric* quantifying the accuracy of the inferred cell growth within a tissue across timepoints, and the *migration metric* quantifying the distance that cells migrate during development under an alignment. We show that DeST-OT produces alignments that are more growth-aware on simulated data. DeST-OT alignments are more biologically realistic in terms of the growth inferred and the distance cells migrate compared to other methods. DeST-OT infers biologically valid cell type transitions on a spatiotemporal dataset of axolotl brain providing insights into the growth dynamics of brain development.

2   Methods

2.1   Formulation

A spatially resolved transcriptomics slice is represented by a tuple $\mathcal{S} = (\mathbf{X}, \mathbf{S})$. $\mathbf{X} \in \mathbb{N}^{n \times p}$ is the transcript count matrix where each row $\mathbf{x}_r$ is the gene expression vector of the corresponding spot, n the number of spots and p the number of genes measured. $\mathbf{S} \in \mathbb{R}^{n \times 2}$ is the spatial position matrix, where the rows $\mathbf{s}_r$ encode the (x, y) coordinates of each spot. Given slices $\mathcal{S}_1 = (\mathbf{X}^{(1)}, \mathbf{S}^{(1)})$ and $\mathcal{S}_2 = (\mathbf{X}^{(2)}, \mathbf{S}^{(2)})$, measured on the same set of genes at timepoints t_1 and t_2, the goal is to derive an alignment matrix $\mathbf{\Pi} \in \mathbb{R}_+^{n_1 \times n_2}$, whose entry $\mathbf{\Pi}_{ij}$ is positive and gives the probability that the cell(s) in spot i of $\mathcal{S}_1$ are the progenitors of the cell(s) in spot j of $\mathcal{S}_2$. The probabilities in the alignment matrix $\mathbf{\Pi}$ are derived to minimize some cost based on the gene expression at each spot and the spatial locations of aligned spots.

We use the mathematical tool of optimal transport (OT) to solve for $\mathbf{\Pi}$. OT finds the most efficient way of moving

mass between two distributions [30], and has previously been applied to single-cell alignment [11, 40] and spatial transcriptomics alignment [24, 45]. We seek to transport the mass of slice $\mathcal{S}_1$ to $\mathcal{S}_2$ where the mass is represented as a distribution over each slice's spots. In the spatiotemporal setting, the amount of mass transferred between a spot at an earlier timepoint and a spot at a later one indicates how probable it is that the former spot is the ancestor of the latter. PASTE [45] uses OT to solve a related problem of static (non-temporal) spatial alignment, in which $\mathcal{S}_1$ and $\mathcal{S}_2$ are adjacent slices of the same tissue from the same timepoint, and minimizes the following objective function:

$$\mathcal{E}_{\text{PASTE}}(\mathbf{\Pi}) = (1-\alpha)\sum_{i,\,j'} \mathbf{C}_{ij'}\mathbf{\Pi}_{ij'} + \alpha \sum_{i,\,j',\,k,\,l'} \left(\mathbf{D}_{ik}^{(1)} - \mathbf{D}_{j'l'}^{(2)}\right)^2 \mathbf{\Pi}_{ij'}\mathbf{\Pi}_{kl'}. \tag{1}$$

This objective function is a convex combination of two terms weighted by a balance parameter α. The first term, which we call the *feature term*, encourages matching spots with similar gene expression, and is also called the Wasserstein term in the OT literature [30]. We use the convention that a prime on an index, e.g. j', refers to a spot in the second slice, while the absence of a prime denotes a spot in the first slice. The ij'-th entry of the matrix $\mathbf{C} \in \mathbb{R}^{n_1 \times n_2}$ is the distance in expression space between expression vector $\mathbf{x}_i$ at $\mathcal{S}_1$-spot i and expression vector $\mathbf{x}'_{j'}$ at $\mathcal{S}_2$-spot j'. The second term, which we call the *spatial term*, encourages matching the intra-slice spatial distance between pairs of spots in each slice, and is called the Gromov-Wasserstein (GW) term [26, 31]. Matrices $\mathbf{D}^{(1)}$ and $\mathbf{D}^{(2)}$ are defined by intra-slice spatial distances $\mathbf{D}_{ij} = \|\mathbf{s}_i - \mathbf{s}_j\|_2$. The convex combination of the feature term and the spatial term is called the *Fused Gromov-Wasserstein* (FGW) objective [38]

PASTE optimizes (1) subject to the following constraints:

$$\begin{aligned} \min \quad & \mathcal{E}_{\text{PASTE}}(\mathbf{\Pi}) \\ s.t. \quad & \mathbf{\Pi}\mathbf{1}_{n_2} = \mathbf{g}_1, \quad \mathbf{\Pi}^T\mathbf{1}_{n_1} = \mathbf{g}_2, \quad \mathbf{\Pi} \geq 0 \end{aligned} \tag{2}$$

where $\mathbf{g}_1 \in \mathbb{R}^{n_1}, \mathbf{g}_2 \in \mathbb{R}^{n_2}$ are uniform probability measures supported on the indices $i \in \{1, \ldots, n_1\}$ and $j' \in \{1, \ldots, n_2\}$; $\mathbf{1}$ is a vector of all one's. These constraints are called *balanced* optimal transport (OT) (Fig. 1b) because the alignment matrix satisfies the marginals $\mathbf{g}_1, \mathbf{g}_2$ strictly.

A recent preprint [21] introduced moscot, a modification of PASTE to use *unbalanced* OT, which is suggested to be helpful for spatiotemporal alignment. Specifically, moscot removes the equality constraints on the marginals, $\mathbf{\Pi}\mathbf{1}_{n_2} = \mathbf{g}_1$, $\mathbf{\Pi}^T\mathbf{1}_{n_1} = \mathbf{g}_2$ of (2), replacing these with two soft constraints in the form of Kullback-Leibler (KL) divergences:

$$\begin{aligned} \min \quad & \mathcal{E}_{\text{PASTE}}(\mathbf{\Pi}) + \frac{\epsilon\tau_a}{1-\tau_a}\text{KL}(\mathbf{\Pi}\mathbf{1}_{n_2}\|\mathbf{g}_1) + \frac{\epsilon\tau_b}{1-\tau_b}\text{KL}(\mathbf{\Pi}^T\mathbf{1}_{n_1}\|\mathbf{g}_2) - \epsilon\text{H}(\mathbf{\Pi}) \\ s.t. \quad & \mathbf{\Pi} \geq 0. \end{aligned} \tag{3}$$

Here $\tau_a, \tau_b \in (0,1)$ are hyperparameters determining the penalty for the marginals deviating from $\mathbf{g}_1$ and $\mathbf{g}_2$. $\text{H}(\cdot)$ is the entropy, where $\text{H}(\mathbf{\Pi}) = -\sum_{i,j'} \mathbf{\Pi}_{ij'}(\log(\mathbf{\Pi}_{ij'}) - 1)$. This entropic regularization accelerates the optimization of $\mathbf{\Pi}$ [9]. moscot has multiple limitations for spatiotemporal alignment. First, the method is supervised: to account for cell growth and death, moscot adjusts $\mathbf{g}_1$ over the first slice using the expression of a predefined set of marker genes, limiting its applicability to organisms and tissues with good prior knowledge. Secondly, the fully unbalanced formulation allows mass to shift around both marginals, limiting the interpretability of the growth information (Supplement § S1.4). Third, the spatial term is not amenable to tissue expansion because it prefers to align identical shapes: $(\mathbf{D}_{ik}^{(1)} - \mathbf{D}_{j'l'}^{(2)})^2 \mathbf{\Pi}_{ij'}\mathbf{\Pi}_{kl'}$ is minimized when the distances inside the square are the same.

DeST-OT uses *semi-relaxed* optimal transport (Fig. 1a) and optimizes a growth-aware objective function modeling different levels of interactions between cells, capturing the growth dynamics comprehensively. In the *semi-relaxed* optimal transport framework (Fig. 1), we relax only the constraint $\mathbf{\Pi}\mathbf{1}_{n_2} = \mathbf{g}_1$ in (2), replacing it by a KL divergence in the objective function, while the other constraint $\mathbf{\Pi}^T\mathbf{1}_{n_1} = \mathbf{g}_2$ is kept. This ensures all of the spots in the second slice are mapped to from the first, while spots in the first slice can contribute a different amount of mass depending on whether they are growing or dying. We set both $\mathbf{g}_1, \mathbf{g}_2$ to assign equal weight $\frac{1}{n_1}$ to each spot. That is, $\mathbf{g}_1$ is the uniform probability measure over spots in $\mathcal{S}_1$, while $\mathbf{g}_2$ is a *positive* measure over spots in $\mathcal{S}_2$. We define an interpretable *growth vector* $\boldsymbol{\xi}$ that represents a mass-flux across the two timepoints indicating the magnitude of growth and death for each spot in $\mathcal{S}_1$,

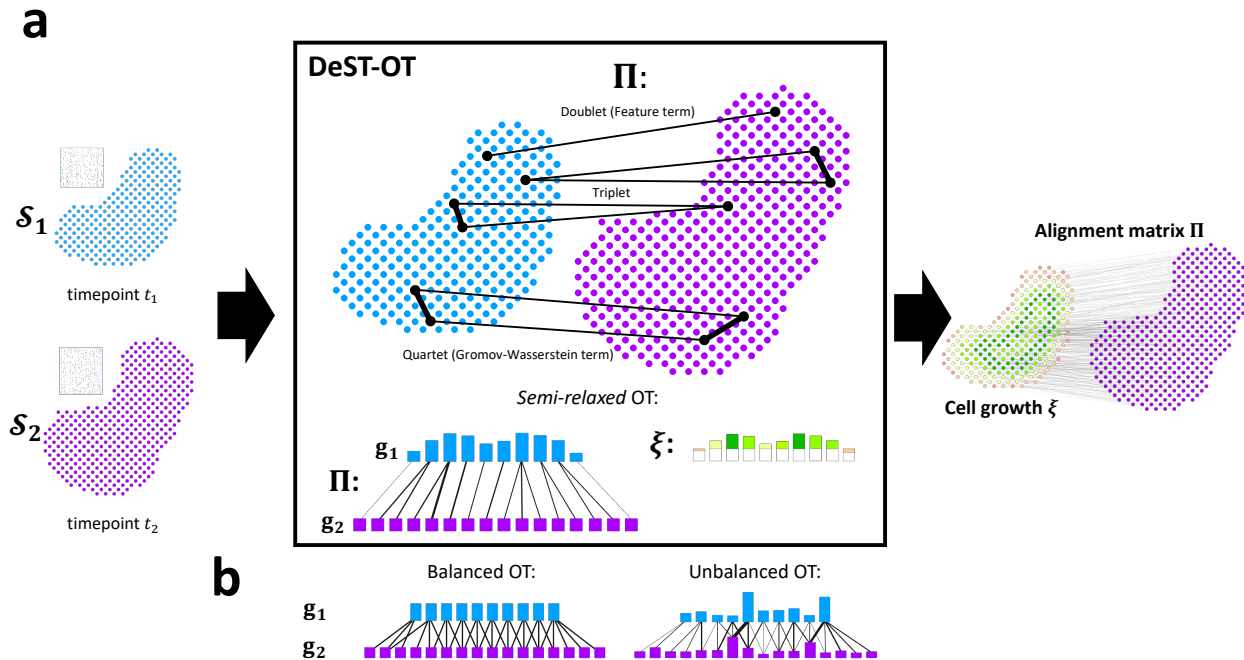$$\boldsymbol{\xi} = \mathbf{\Pi}\mathbf{1}_{n_2} - \mathbf{g}_1. \tag{4}$$

a

b

Figure 1: Overview of DeST-OT and semi-relaxed optimal transport (OT). (a) Given a pair of $\mathcal{S}_1$ and $\mathcal{S}_2$ from timepoints t_1 and t_2, respectively, DeST-OT infers an alignment matrix $\mathbf{\Pi}$ and a growth vector $\boldsymbol{\xi} = \mathbf{\Pi}\mathbf{1}_{n_2} - \mathbf{g}_1$ by solving a semi-relaxed optimal transport problem with doublet, triplet, quartet objective costs. Green entries in $\boldsymbol{\xi}$ indicate cell growth while red entries indicate death (b) Balanced OT, which fixes both marginals $\mathbf{g}_1, \mathbf{g}_2$, and unbalanced OT, which varies both marginals.

The growth vector $\boldsymbol{\xi} \in \mathbb{R}^{n_1}$ is the change in mass relative to a uniform prior $\mathbf{g}_1$ at each spot. The total sum of the entries of $\boldsymbol{\xi}$ is therefore $\frac{n_2 - n_1}{n_1}$, fixed in proportion to the total change of mass across slices. For a spot i at time t_1, $\boldsymbol{\xi}_i > 0$ means that spot i has > 1 descendant in the second slice, and correspondingly, $\boldsymbol{\xi}_i < 0$ implies spot i has < 1 descendant in the second slice. The growth vector $\boldsymbol{\xi}$ is a change in mass over time – to convert this into a growth rate, one can take $J = \log(1 + n_1\boldsymbol{\xi})/(t_2 - t_1)$ (Supplement § S2). See Supplement § S1.4 and § S3 for further discussion of the growth vector $\boldsymbol{\xi}$.

DeST-OT optimizes a growth-aware objective function subject to the semi-relaxed constraints. The objective cost of DeST-OT for finding an optimal spatiotemporal alignment matrix $\mathbf{\Pi}$ consists of three terms: a doublet term, a triplet term, and a quartet term. The doublet term, $\sum_{i,j'} \mathbf{C}_{ij'}\mathbf{\Pi}_{ij'}$, is the same as the feature term in PASTE, where $\mathbf{C} \in \mathbb{R}^{n_1 \times n_2}$ is an inter-slice gene expression distance matrix. The term compares the expression of two spots, one from each slice, hence we call it the *doublet* term of our objective.

The *quartet* term compares spot-pairs, with one pair from each slice. The quartet term is defined as $\sum_{i,j',k,l'}(\mathbf{M}_{ik}^{(1)} - \mathbf{M}_{j'l'}^{(2)})^2 \mathbf{\Pi}_{ij'}\mathbf{\Pi}_{kl'}$, where each matrix $\mathbf{M}^{(i)}$ is defined to be the entrywise product of the square matrices $\mathbf{C}^{(i)}$ and $\mathbf{D}^{(i)}$. $\mathbf{C}^{(i)} \in \mathbb{R}^{n_i \times n_i}$ is the distance in the expression space between each pair of spots on slice i. $\mathbf{D}^{(i)}$ is the intra-slice spatial distance matrix as in PASTE. The quartet term is equivalent to the spatial (GW) term of both PASTE and moscot but with matrices $\mathbf{M}^{(i)}$ that jointly model transcriptomic and spatial information, and with the semi-relaxed constraint applied to the gradient (Supplement § S4). We refer to $\mathbf{M}$ as *merged feature-spatial matrices*. While the spatial distance matrices $(\mathbf{D}^{(1)}, \mathbf{D}^{(2)})$ are appropriate for static alignment, they encode a rigid geometry that does not account for spatial deformations accompanying growth. On the contrary, DeST-OT matches a more flexible feature-smoothed geometry between the two slices, accounting for expansion or shrinkage of tissues during development.

The *triplet* term models the ancestor-descendant relationship between a single ancestor spot and multiple descendent spots, an essential relationship in growing tissues that is not well modeled by the other terms. When an ancestor spot differentiates into multiple descendant spots, these descendant spots should be close to each other in both physical space and feature space. Correspondingly, multiple ancestors should also be close. We make this notion precise by adding a *triplet* term to our objective: $\mathcal{E}_{\text{triplet}}(\mathbf{\Pi}) = \sum_{ij'k'} \mathbf{\Pi}_{ij'}\mathbf{\Pi}_{ik'}\mathbf{M}_{j'k'}^{(2)2} + \sum_{ijk} \mathbf{\Pi}_{ik'}\mathbf{\Pi}_{jk'}\mathbf{M}_{ij}^{(1)2}$. The entrywise squares on the $\mathbf{M}$ matrices match the form of the quartet term, upweighting the triplet summands which enforce the similarity

of descendants and ancestors. Adding these terms to our objective function has a regularizing effect: $\mathbf{\Pi}$ is penalized for predicting distant descendants j', k' of the same spot i in the first slice, or for predicting distant ancestors i, j of the same spot k' in the second slice. Distance is interpreted to be both spatial and transcriptomic due to the merged feature-spatial $\mathbf{M}$ matrices.

We call the sum $\mathcal{E}^{\mathbf{M}}$ of the triplet term and the quartet term the *merged feature-spatial* term, since both use merged feature-spatial matrices and encourage alignments to respect developmental dynamics in both physical space and gene expression space. Specifically, we define

$$\mathcal{E}^{\mathbf{M}}(\mathbf{\Pi}) = \frac{1}{2}\left(\underbrace{\sum_{i,j',k'} \mathbf{\Pi}_{ij'}\mathbf{\Pi}_{ik'}\mathbf{M}_{j'k'}^{(2)2} + \sum_{i,j,k'} \mathbf{\Pi}_{ik'}\mathbf{\Pi}_{jk'}\mathbf{M}_{ij}^{(1)2}}_{\text{triplet}} + \underbrace{\sum_{i,j',k,l'} (\mathbf{M}_{ik}^{(1)} - \mathbf{M}_{j'l'}^{(2)})^2 \mathbf{\Pi}_{ij'}\mathbf{\Pi}_{kl'}}_{\text{quartet}}\right). \quad (5)$$

Combining all of the above, the DeST-OT objective function is:

$$\mathcal{E}_{\text{DeST-OT}} = (1-\alpha)\underbrace{\sum_{i,j'} \mathbf{C}_{ij'}\mathbf{\Pi}_{ij'}}_{\text{doublet}} + \alpha\mathcal{E}^{\mathbf{M}}(\mathbf{\Pi}) \quad (6)$$

The combination of the doublet, triplet, and quartet terms captures lower to higher order of interactions between spots in a growing tissue (Fig. 1a). The DeST-OT optimization problem, with entropic regularization and the semi-relaxed constraints is

$$\begin{aligned} \min \quad & \mathcal{E}_{\text{DeST-OT}}(\mathbf{\Pi}) + \gamma \text{KL}(\mathbf{\Pi}\mathbf{1}_{n_2} \parallel \mathbf{g}_1) - \epsilon \text{H}(\mathbf{\Pi}) \\ s.t. \quad & \mathbf{\Pi}^T\mathbf{1}_{n_1} = \mathbf{g}_2, \quad \mathbf{\Pi} \geq 0 \end{aligned} \quad (7)$$

The balance parameter α balances the contribution of the feature term and the merged feature-spatial term to the alignment. γ governs the compliance of the semi-relaxed constraint, and ϵ governs the strength of entropic regularization. We discuss the effect of these hyperparameters in the Results section.

2.2 Optimization Using Sinkhorn

We solve the DeST-OT optimization problem by deriving a variant of the Sinkhorn algorithm, which has become the canonical way to compute OT alignments due to its speed [9]. One may convert an optimal transport problem with a general objective into the framework of Sinkhorn by adding an entropy regularization $-\epsilon \text{H}(\mathbf{\Pi})$ to the objective function. Following the framework of Sinkhorn, the DeST-OT optimization problem (7) includes an entropy regularization term and we derive a set of updates from the KKT conditions for the semi-relaxed constraints to solve for $\mathbf{\Pi}$. In practice, we take the dual of the semi-relaxed optimization to convert these updates into the log-domain [35], avoiding numerical overflow. The details of the optimization procedure are discussed in Supplement § S4.

2.3 Assessing alignment quality by cellular growth and migration

The true spatiotemporal alignment is often unknown, making it difficult to evaluate the accuracy of an alignment. We introduce two metrics to quantify the plausibility of an alignment: the *growth distortion metric* and the *migration metric*. The growth distortion quantifies the difference between the inferred growth and the proportional change of cell types in the two slices, given cell type labels for each spot in both slices. The migration metric quantifies how far cells "move" from the first timepoint to the second in a common coordinate framework describing the actual tissue. We say that an alignment $\mathbf{\Pi}$ is biologically valid when its growth distortion is ≈ 0, and physically valid if the migration distance is low.

2.3.1 A metric of growth distortion

Given an alignment matrix $\mathbf{\Pi}$, we define the *growth distortion metric* to quantify how well the growth vector $\boldsymbol{\xi}$ defined by equation (4) matches the observed change in proportion of given cell type labels over both slices. Formally, we are given a partition $\mathcal{P}_1 = (\mathcal{P}_1(p))_{p=1}^P$ of spots in slice 1, where the set $\mathcal{P}_1(p)$ consists of all spots of cell type p at time t_1, and a partition $\mathcal{P}_2 = (\mathcal{P}_2(p))_{p=1}^P$ of spots at timepoint t_2. The mass $m_1(p)$ of cell type p at time t_1 is $m_1(p) = |\mathcal{P}_1(p)|$, the number of t_1-spots with the label p. Likewise, the mass $m_2(p)$ of cell type p at time t_2 is $m_2(p) = |\mathcal{P}_2(p)|$. The change-in-mass for cell type p across these two timepoints is then $m_2(p) - m_1(p)$. To ensure that mass change has

the same scale as the growth vector $\boldsymbol{\xi}$, we normalize the change-in-mass as $\frac{m_2(p)-m_1(p)}{n_1}$ since $\texttt{DeST-OT}$ marginals assign mass $\frac{1}{n_1}$ to each spot, while the counting measure used to define the $m_t(p)$ assigns mass 1 to each spot.

We define the growth distortion metric under two assumptions: first, that there are no cell type transitions between distinct cell types (we discuss how to relax this assumption shortly). Second, the burden of accomplishing the change in mass is shared equally across cells of the same type. This second assumption can be viewed as an entropy-maximizing assumption. Under these two assumptions, the "true" growth $\gamma(p)$ at any $i \in \mathcal{P}_1(p)$ is

$$\gamma(p) = \frac{1}{m_1(p)} \left(\frac{m_2(p) - m_1(p)}{n_1} \right). \tag{8}$$

Note that summing these values over all t_1-spots yields $\frac{n_2-n_1}{n_1}$, the total (normalized) change in mass across the two slices (Supplement § S5.1). The *growth distortion metric* $\mathcal{J}_{growth}$ of an alignment matrix $\boldsymbol{\Pi}$ with its associated $\boldsymbol{\xi}$, relative to cell type partitions $\mathcal{P}_1$ and $\mathcal{P}_2$, measures the total distortion between the inferred growth $\boldsymbol{\xi}$ and the true growth γ at each spot:

$$\mathcal{J}_{growth} = \sum_{p=1}^{P} \sum_{i \in \mathcal{P}_1(p)} \|\boldsymbol{\xi}_i - \gamma(p)\|_2^2. \tag{9}$$

We generalize the growth distortion metric to the case when cell type transitions are present (but unknown) using a reverse-time transition matrix $\mathbf{T} \in \mathbb{R}^{P \times P}$. This matrix acts on a vector of cell type masses, redistributing the mass $\mathbf{m}_2$ at time t_2 to the ancestral cell types at t_1 via the update $\mathbf{m}_1 = \mathbf{T}\mathbf{m}_2$. To compute the growth distortion metric for an alignment matrix $\boldsymbol{\Pi}$, we use the following cell type transition matrix $\mathbf{T}$:

$$\mathbf{T}_{pq} = \left(\frac{n_1}{m_2(q)} \right) \sum_{i \in \mathcal{P}_1(p)} \sum_{j' \in \mathcal{P}_2(q)} \boldsymbol{\Pi}_{ij'}, \tag{10}$$

and prove in Proposition 2 of Supplement § S5.2 that the above $\mathbf{T}$ minimizes $\mathcal{J}_{growth}$ for a given $\boldsymbol{\Pi}$ across all $\mathbf{T}$'s. That is, when we do not know the true cell type transitions, we compute the growth distortion of an alignment as the lowest distortion it could possibly achieve under any cell type transition.

2.3.2 A metric of cell migration

We introduce a migration metric $\mathcal{J}_{migration}$ of an alignment $\boldsymbol{\Pi}$ between two slices that quantifies the distance cells move under the alignment. This metric formalizes the intuition that the descendants of a cell tend to be close to their parent, particularly over short time intervals. Given an alignment $\boldsymbol{\Pi}$ and function $\varphi : \mathbb{R}^2 \to \mathbb{R}^2$ that places slice $\mathcal{S}_2$ into a common-coordinate frame with slice $\mathcal{S}_1$, we define the *migration metric* as:

$$\mathcal{J}_{migration} = \mathbb{E}_{(i,j') \sim \boldsymbol{\Pi}} \left[\|\mathbf{s}_i - \varphi(\mathbf{s}_{j'})\|_2^2 \right], \tag{11}$$

namely the average squared distance between spatial coordinate $\mathbf{s}_i$ in slice $\mathcal{S}_1$ and transformed second-slice spatial coordinate $\varphi(\mathbf{s}_{j'})$ over pairs (i, j') that are sampled proportionally to $\boldsymbol{\Pi}$ (column normalizing $\boldsymbol{\Pi}$, as in Supplement Eq. (49)). In the results reported below, we use the function $\varphi(\mathbf{z}) = \mathbf{Q}(\mathbf{z} - \mathbf{h})$ for an orthogonal transformation $\mathbf{Q}$ and translation vector $\mathbf{h} \in \mathbb{R}^2$ that solve a generalized Procrustes' problem (Supplement § S6). This describes a rigid-body transformation relating the coordinate frames of slice $\mathcal{S}_1$ and $\mathcal{S}_2$.

3 Results

3.1 Evaluation on simulated ST data

We evaluated $\texttt{DeST-OT}$ and $\texttt{moscot}$ on simulated data from one- and two-dimensional tissue slices with eight-dimensional feature expressions for each spot. For each timepoint, the feature at each spot varies within each cell type. Details of the simulation of features are in Supplement § S7. Since $\texttt{moscot}$ assumes the marginals used as input to its OT problem are already adapted to cell proliferation and apoptosis using prior knowledge, we set $\texttt{moscot}$'s marginal over t_1 to account for changing cell type proportion in each experiment. $\texttt{DeST-OT}$ uses semi-relaxed OT, and thus no prior knowledge of growth and death was required.

The first simulated dataset consisted of a pair of one-dimensional tissue slices, denoted as timepoint t_1 and t_2, each with 101 spots. There were two cell types across both slices. Slice t_1 had 30 spots of cell type A and 71 spots of cell type B; slice t_2 had 60 spots of cell type A and 41 spots of cell type B (Fig. 2ab). Therefore, cell type A grew by a factor of 2 from t_1 to t_2 and cell type B shrunk by roughly the same factor. We ran both $\texttt{DeST-OT}$ and $\texttt{moscot}$ on this pair of
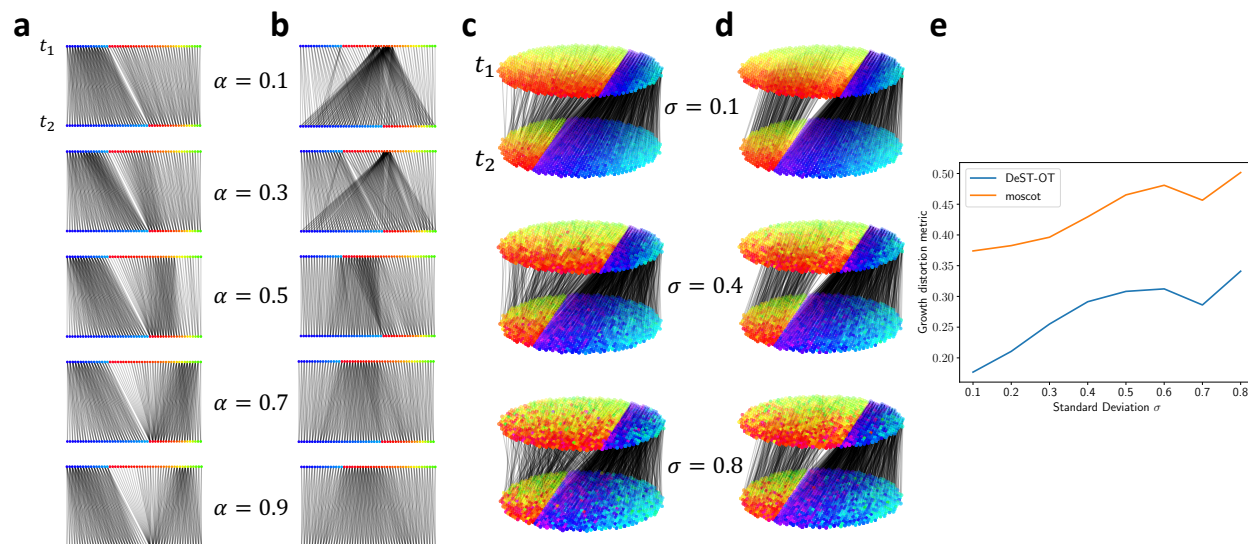
Figure 2: DeST-OT and moscot alignments on simulated data. a, DeST-OT and **b**, moscot alignment results for the balance parameter α ranging from 0.1 (mostly feature term) to 0.9 (mostly spatial terms), on 1D simulated slices. DeST-OT's alignments indicate the cell type boundary, and color represents the polar angle made from two of the four non-zero coordinates in each cell type. **c**, DeST-OT and **d**, moscot alignments on 2D simulated slices with standard deviation of the expression noise $\sigma = 0.1, 0.4, 0.8$. Expression features are visualized similarly in 2D. **e**, The growth distortion metric for DeST-OT and moscot as a function of σ.

one-dimensional slices, varying the balance parameter α in the objective functions from $\alpha = 0.1$ to $\alpha = 0.9$, gradually placing more weight on each method's spatial term (i.e. the merged feature-spatial term in DeST-OT, and the GW term in moscot) in the objective. We found that DeST-OT alignments are robust to varying α, always aligning cells to the correct cell types across timepoints (Fig. 2a). DeST-OT captures the true growth pattern of cells for all values of α because the merged feature-spatial term of DeST-OT incorporates both transcriptional and spatial information. On the other hand, moscot has greater difficulty capturing growing and shrinking cell types with larger α, as its spatial term emphasizes matching the shapes of the two slices as discussed in §2.1 (Fig. 2b). This demonstrates the effectiveness of DeST-OT's spatiotemporal objective function, as well as the importance of DeST-OT's semi-relaxed framework even when aligning slices with the same number of spots.

We next tested DeST-OT and moscot on a more realistic simulation with two-dimensional slices and feature expression noise. We generated two elliptical slices at t_1 and t_2 of the same size (988 spots), again with two cell types across the slices; cell type A occupies the right regions of the slices in (Fig. 2b), while cell type B is on the left. Slice t_1 had 240 spots of cell type A and 748 spots of cell type B; slice t_2 had 726 spots of cell type A and 262 spots of cell type B. Each cell type is characterized by a pair $\mathbf{f}_{x,\text{right}}, \mathbf{f}_{x,\text{left}}$ of eight-dimensional feature vectors for the x-direction, and another pair $\mathbf{f}_{y,\text{top}}, \mathbf{f}_{y,\text{bottom}}$ of feature vectors for the y-direction. The feature at a given spot in each cell type is a convex combination $\mathbf{f}(x,y) = \lambda_x \mathbf{f}_{x,\text{right}} + (1 - \lambda_x)\mathbf{f}_{x,\text{left}} + \lambda_y \mathbf{f}_{y,\text{top}} + (1 - \lambda_y)\mathbf{f}_{y,\text{bottom}}$ of the x-direction feature vectors the y-direction feature vectors. The coefficients λ_x, λ_y are determined by the horizontal and vertical distance to the spot's cell type boundary. This creates a consistent gradient of features within each cell type (Supplement § S7). For $(x_1, y_1) \in \mathbf{S}^{(1)}$, $(x_2, y_2) \in \mathbf{S}^{(2)}$ we have that if $\lambda_{x_1}^A = \lambda_{x_2}^A$ and $\lambda_{y_1}^A = \lambda_{y_2}^A$ then $\mathbf{f}_A(x_1, y_1) = \mathbf{f}_A(x_2, y_2)$ and the two spots should be aligned between timepoints 1 and 2 (likewise for cell type B). We then added zero-centered Gaussian noise with standard deviation σ independently to each feature dimension, with σ ranging from 0.1 to 0.8 in increments of 0.1. In addition to supplying moscot with the ground-truth adapted t_1-marginal, we also set it to be fully unbalanced with $\tau_a = 0.99, \tau_b = 0.999$ as suggested by the tutorial for noisy data.

DeST-OT aligns ancestor cells to descendant cells correctly along the cell type feature gradients across timepoints (Fig. 2c), capturing cell growth and death. DeST-OT alignments are robust to noise as well, aligning cell types correctly even with added noise in spot features. While moscot produces straighter alignments (Fig. 2d) we found that it identifies the ancestors of cell type B at t_2 to come from a small, similarly shaped region of cell type A at t_1 even with perfect growth knowledge encoded in the marginal $\mathbf{g}_1$. Rather than aligning along a gradient of spatially expanding features, moscot's spatial term prefers to align identical shapes, and is not suited to aligning tissue slices which grow and deform over time. DeST-OT consistently infers more accurate cell development as quantitatively shown by the
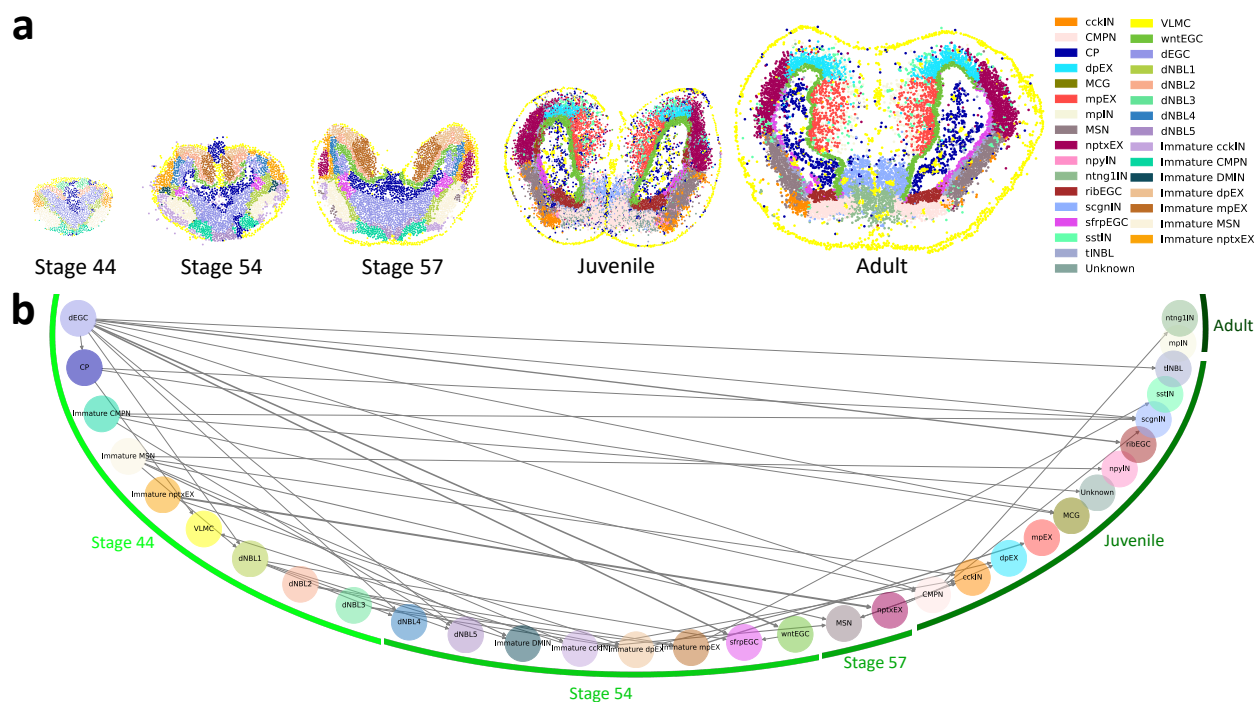
6

Figure 3: `DeST-OT` analysis of axolotl brain development. a, Stereo-seq data from axolotl brain sections at embryonic stage 44, embryonic stage 54, embryonic stage 57, Juvenile stage, and Adult stage, with cell type labels from [43] **b**, Cell type transition graph derived from `DeST-OT` alignments throughout axolotl brain development. The cell types are arranged in a half circle. A cell type is assigned to a developmental stage if it first appears in that stage. The width of the edges are proportional to the weight of transition. Self-loops are omitted.

growth distortion metric (Fig. 2e).

3.2 Axolotl brain development

We applied `DeST-OT` to analyze the developmental dynamics of the telencephalon, a region of the brain, in axolotl (*Ambystoma mexicanum*), a species of salamander. *Wei et. al.* [43] used Stereo-seq [5] to measure gene expression in the axolotl telencephalon at five development timepoints: three embryonic stages (44, 54, 57), Juvenile stage, and Adult stage (Fig. 3a). The slices grow in size, and progenitor cell types transition into mature cell types during the developmental process. We used `DeST-OT`, `moscot`, `PASTE`, `STalign`, and `SLAT` to infer an alignment between each pair of timepoints respectively, and computed the growth distortion and migration metric for each method (Fig. 4). Since new cell types appear at individual timepoints and the transitions between cell type during development are not annotated, we computed the growth distortion metric for each method under the cell type transition that minimizes their growth distortion as described in § 2.3. `DeST-OT` has the lowest growth distortion among all methods while maintaining low migration distances, demonstrating the quality of the `DeST-OT` alignments (Fig. 4). `moscot` and `STalign` achieve a low migration metric by shape-matching but have high growth distortions. `SLAT` has a low migration distance on this dataset as well, but cannot estimate cell growth and death accurately either.

We examined the cell type transition matrix $\mathbf{T}$ between each pair of adjacent timepoints derived from the `DeST-OT` alignment (§ 2.3) and the cell type annotations from [43] (Fig. S1). From these transition matrices, we derive a weighted directed graph showing all frequent transitions (>20%) (Fig. 3b). Many of the `DeST-OT` inferred cell type transitions are consistent with previously reported developmental trajectories. For example, we found that among all cell types, dEGCs (developmental ependymoglial cells) give rise to the largest number (11) of descendent cell types, consistent with previous studies which suggest that EGCs are equivalent to neural stem cells in mammals and contribute to neurogenesis during brain development [19, 20, 3]. Furthermore, immature cell types expressing early developmental markers disappear from the juvenile stage onward (Fig. 3a), and `DeST-OT` confirmed that immature cells of each cell type, such as CMPN or nptxEX, transition into their respective mature cell types. Previous studies suggested a potential lineage transition from EGCs to neuroblasts (NBLs) [29], and a transition from dEGC to NBL cell types that
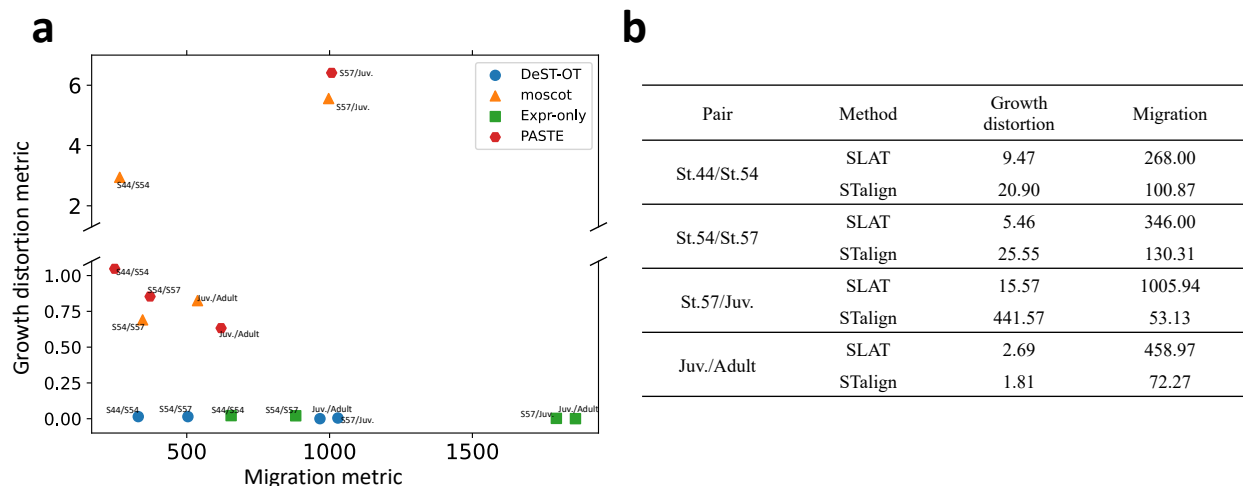
7

Figure 4: Alignment performance of various methods on the axolotl brain development dataset. a, The growth distortion metric and migration metric of `DeST-OT`, `moscot`, `Expr-only`, `PASTE` alignments on all pairs of axolotl brain development timepoints. **b**, The growth distortion and migration metric of `SLAT` and `STalign` alignments on all pairs of axolotl brain development timepoints. Not included in the plot in **a** because of high growth distortion.

appear after stage 44 (dNBL4, dNBL5, tlNBL) is also found by `DeST-OT`. Finally, dEGCs disappear at stage 57, and `DeST-OT` predicts that it transitions mostly into ribEGCs located in the ventricular zone, which is the same spatial region where dEGCs located before and consistent with the findings in [43]. We observe a directed cycle between cckIN and MSN, probably because the two cell types are mixed together in the striatum region. There is no directed edge going into mpIN because it has multiple progenitor cell types and no cell type passes the threshold (20% in this case) for including an edge giving rise to mpIN (Fig. S1), indicating a diverse origin of mpIN.

We found that the growth patterns of individual cells inferred by `DeST-OT` are more biologically reasonable than those inferred by `moscot` (Fig. 5). For the three embryonic stages, `DeST-OT` infers that all cells are growing and identifies differential growth patterns of tissue regions: the outer part of the telencephalon, mostly occupied by immature cell types, grows faster than the inner part. In contrast, the growth patterns inferred by `moscot` tend to be sparser, with a few "representative" cells have a high growth and thus a large number of descendants in the next timepoint, while most other cells are dying, which is not realistic for embryonic tissues. This is a computational artifact of the fully unbalanced OT formulation which allows a few "best" cells from the two slices to be aligned, hence does not fit spatiotemporal data where all descendant spots should be aligned.

4 Discussion

We introduce `DeST-OT`, a method for aligning spatiotemporal transcriptomics data and for inferring cell proliferation and apoptosis. Using a semi-relaxed optimal transport framework and an objective cost designed for spatiotemporal data, `DeST-OT` finds an alignment between progenitor and descendent cells in developmental spatial transcriptomics data, infers growth and death rates, and infers cell type transitions during tissue development. To quanitfy the performance of `DeST-OT` and other spatiotemporal alignment methods, we introduce the migration metric to quantify the distance cells travel under a spatiotemporal alignment and the growth distortion metric to quantify how accurately an alignment infers growth relative to ground-truth cell type annotations. We show on simulated data that `DeST-OT` outperforms other methods and infers cell growth and death accurately. We use `DeST-OT` to study axolotl brain development and confirm previously reported lineage transitions. `DeST-OT` alignments can elucidate developmental dynamics and may lay the ground for the discovery of their molecular basis. We also demonstrate that `DeST-OT` alignments are more biologically and physically realistic than competing methods.

Future work includes the evaluation of `DeST-OT` on other spatiotemporal datasets. There are currently few such publicly available datasets, but analysis of another unpublished dataset is ongoing and will be included in a future revision. `DeST-OT` will be a useful tool for biologists to gain new insights in spatiotemporal processes such as development and reprogramming, discovering new temporally and spatially dependent biological phenomena.

8

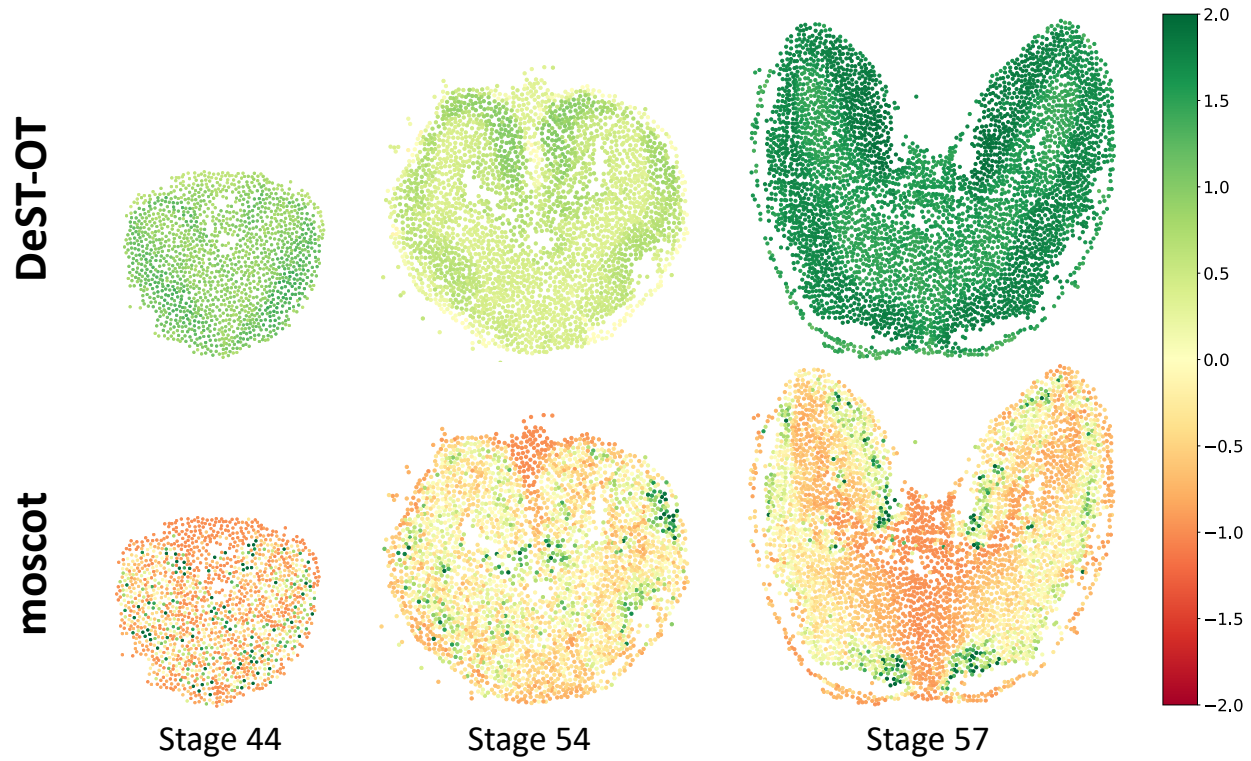**Figure 5: Growth patterns of axolotl brain.** The growth of cells inferred by `DeST-OT` and `moscot` on the three embryonic stages of axolotl brain development. Growth vector ξ is normalized to unit of number of cells.

5   Acknowledgements

References

[1] Chiara Baccin, Jude Al-Sabah, Lars Velten, Patrick M Helbling, Florian Grünschläger, Pablo Hernández-Malmierca, César Nombela-Arrieta, Lars M Steinmetz, Andreas Trumpp, and Simon Haas. Combined single-cell and spatial transcriptomics reveal the molecular, cellular and spatial bone marrow niche organization. *Nature cell biology*, 22(1):38–48, 2020.

[2] Jean-David Benamou. Numerical resolution of an "unbalanced" mass transport problem. *ESAIM: Mathematical Modelling and Numerical Analysis*, 37(5):851–868, 2003.

[3] Daniel A Berg, Matthew Kirkham, Anna Beljajeva, Dunja Knapp, Bianca Habermann, Jesper Ryge, Elly M Tanaka, and András Simon. Efficient regeneration by activation of neurogenesis in homeostatically quiescent regions of the adult vertebrate brain. *Development*, 137(24):4127–4134, 2010.

[4] Mathieu Blondel, Vivien Seguy, and Antoine Rolet. Smooth and sparse optimal transport. In *International conference on artificial intelligence and statistics*, pages 880–889. PMLR, 2018.

[5] Ao Chen, Sha Liao, Mengnan Cheng, Kailong Ma, Liang Wu, Yiwei Lai, Xiaojie Qiu, Jin Yang, Jiangshan Xu, Shijie Hao, et al. Spatiotemporal transcriptomic atlas of mouse organogenesis using dna nanoball-patterned arrays. *Cell*, 185(10):1777–1792, 2022.

[6] Yongxin Chen, Tryphon T Georgiou, Michele Pavon, and Allen Tannenbaum. Relaxed schrödinger bridges and robust network routing. *IEEE transactions on control of network systems*, 7(2):923–931, 2019.

[7] Lénaïc Chizat, Gabriel Peyré, Bernhard Schmitzer, and François-Xavier Vialard. Unbalanced optimal transport: Dynamic and kantorovich formulations. *Journal of Functional Analysis*, 274(11):3090–3123, 2018.

[8] Kalen Clifton, Manjari Anant, Gohta Aihara, Lyla Atta, Osagie K Aimiuwu, Justus M Kebschull, Michael I Miller, Daniel Tward, and Jean Fan. Alignment of spatial transcriptomics data using diffeomorphic metric mapping. *bioRxiv*, pages 2023–04, 2023.

[9] Marco Cuturi. Sinkhorn distances: Lightspeed computation of optimal transport. *Advances in Neural Information Processing Systems*, pages 2292–2300, 2013.

[10] Anton HJ de Ruiter and James Richard Forbes. On the solution ofwahba's problem on so (n). *The Journal of the Astronautical Sciences*, 60:1–31, 2013.

[11] Pinar Demetci, Rebecca Santorella, Björn Sandstede, William Stafford Noble, and Ritambhara Singh. Scot: single-cell multi-omics alignment with optimal transport. *Journal of Computational Biology*, 29(1):3–18, 2022.

[12] Shunjie Dong, Zixuan Pan, Yu Fu, Dongwei Xu, Kuangyu Shi, Qianqian Yang, Yiyu Shi, and Cheng Zhuo. Partial unbalanced feature transport for cross-modality cardiac image segmentation. *IEEE Transactions on Medical Imaging*, 2023.

[13] Takumi Fukunaga and Hiroyuki Kasai. Fast block-coordinate frank-wolfe algorithm for semi-relaxed optimal transport. *arXiv preprint arXiv:2103.05857*, 2021.

[14] Takumi Fukunaga and Hiroyuki Kasai. On the convergence of semi-relaxed sinkhorn with marginal constraint and ot distance gaps. *arXiv preprint arXiv:2205.13846*, 2022.

[15] A. Garcia-Bellido and J.R. Merriam. Parameters of the wing imaginal disc development ofDrosophila melanogaster. *Developmental Biology*, 24(1):61–87, January 1971.

[16] Geoffrey E. Hinton. Training products of experts by minimizing contrastive divergence. *Neural Computation*, 14(8):1771–1800, August 2002.

[17] Andrew L Ji, Adam J Rubin, Kim Thrane, Sizun Jiang, David L Reynolds, Robin M Meyers, Margaret G Guo, Benson M George, Annelie Mollbrink, Joseph Bergenstråhle, et al. Multimodal analysis of composition and spatial architecture in human squamous cell carcinoma. *Cell*, 182(2):497–514, 2020.

[18] Andrew Jones, F. William Townes, Didong Li, and Barbara E. Engelhardt. Alignment of spatial genomics data using deep gaussian processes. *Nature Methods*, 20(9):1379–1387, August 2023.

[19] Alberto Joven and András Simon. Homeostatic and regenerative neurogenesis in salamanders. *Progress in neurobiology*, 170:81–98, 2018.

[20] Matthew Kirkham, L Shahul Hameed, Daniel A Berg, Heng Wang, and András Simon. Progenitor cell dynamics in the newt telencephalon during homeostasis and neuronal regeneration. *Stem cell reports*, 2(4):507–519, 2014.

[21] Dominik Klein, Giovanni Palla, Marius Lange, Michal Klein, Zoe Piran, Manuel Gander, Laetitia Meng-Papaxanthos, Michael Sterr, Aimée Bastidas-Ponce, Marta Tarquis-Medina, Heiko Lickert, Mostafa Bakhti, Mor Nitzan, Marco Cuturi, and Fabian J. Theis. Mapping cells through time and space with moscot. *bioRxiv*, 2023.

[22] Hugo Lavenant, Stephen Zhang, Young-Heon Kim, and Geoffrey Schiebinger. Towards a mathematical theory of trajectory inference. *arXiv preprint arXiv:2102.09204*, 2021.

[23] Yingxin Lin and Jean YH Yang. 3d reconstruction of spatial expression. *Nature Methods*, 19(5):526–527, 2022.

[24] Xinhao Liu, Ron Zeira, and Benjamin J Raphael. Partial alignment of multislice spatially resolved transcriptomics data. *Genome Research*, 33(7):1124–1132, 2023.

[25] Cristina Martín-Castellanos and Bruce A Edgar. A characterization of the effects of dpp signaling on cell growth and proliferation in the drosophila wing. 2002.

[26] Facundo Mémoli. Gromov–wasserstein distances and the metric approach to object matching. *Foundations of computational mathematics*, 11:417–487, 2011.

[27] M Milán, S Campuzano, and A García-Bellido. Cell cycling and patterned cell proliferation in the wing primordium of drosophila. *Proceedings of the National Academy of Sciences*, 93(2):640–645, January 1996.

[28] Lambda Moses and Lior Pachter. Museum of spatial transcriptomics. *Nature Methods*, 19(5):534–546, 2022.

[29] Stephen C Noctor, Alexander C Flint, Tamily A Weissman, Ryan S Dammerman, and Arnold R Kriegstein. Neurons derived from radial glial cells establish radial units in neocortex. *Nature*, 409(6821):714–720, 2001.

[30] Gabriel Peyré, Marco Cuturi, et al. Computational optimal transport: With applications to data science. *Foundations and Trends® in Machine Learning*, 11(5-6):355–607, 2019.

[31] Gabriel Peyré, Marco Cuturi, and Justin Solomon. Gromov-wasserstein averaging of kernel and distance matrices. In *International conference on machine learning*, pages 2664–2672. PMLR, 2016.

[32] Julien Rabin, Sira Ferradans, and Nicolas Papadakis. Adaptive color transfer with relaxed optimal transport. In *2014 IEEE international conference on image processing (ICIP)*, pages 4852–4856. IEEE, 2014.

[33] Anjali Rao, Dalia Barkley, Gustavo S França, and Itai Yanai. Exploring tissue architecture using spatial transcriptomics. *Nature*, 596(7871):211–220, 2021.

[34] Geoffrey Schiebinger, Jian Shu, Marcin Tabaka, Brian Cleary, Vidya Subramanian, Aryeh Solomon, Joshua Gould, Siyan Liu, Stacie Lin, Peter Berube, et al. Optimal-transport analysis of single-cell gene expression identifies developmental trajectories in reprogramming. *Cell*, 176(4):928–943, 2019.

[35] Bernhard Schmitzer. Stabilized sparse scaling algorithms for entropy regularized transport problems. *SIAM Journal on Scientific Computing*, 41(3):A1443–A1481, January 2019.

[36] Thibault Séjourné, Gabriel Peyré, and François-Xavier Vialard. Unbalanced optimal transport, from theory to numerics. *arXiv preprint arXiv:2211.08775*, 2022.

[37] Patrik L Ståhl, Fredrik Salmén, Sanja Vickovic, Anna Lundmark, José Fernández Navarro, Jens Magnusson, Stefania Giacomello, Michaela Asp, Jakub O Westholm, Mikael Huss, et al. Visualization and analysis of gene expression in tissue sections by spatial transcriptomics. *Science*, 353(6294):78–82, 2016.

[38] Vayer Titouan, Nicolas Courty, Romain Tavenard, and Rémi Flamary. Optimal transport for structured data with application on graphs. In *International Conference on Machine Learning*, pages 6275–6284. PMLR, 2019.

[39] Alexander Tong, Jessie Huang, Guy Wolf, David Van Dijk, and Smita Krishnaswamy. TrajectoryNet: A dynamic optimal transport network for modeling cellular dynamics. In Hal Daumé III and Aarti Singh, editors, *Proceedings of the 37th International Conference on Machine Learning*, volume 119 of *Proceedings of Machine Learning Research*, pages 9526–9536. PMLR, 13–18 Jul 2020.

[40] Quang Huy Tran, Hicham Janati, Nicolas Courty, Rémi Flamary, Ievgen Redko, Pinar Demetci, and Ritambhara Singh. Unbalanced co-optimal transport. In *Proceedings of the AAAI Conference on Artificial Intelligence*, volume 37, pages 10006–10016, 2023.

[41] Cédric Vincent-Cuaz, Rémi Flamary, Marco Corneli, Titouan Vayer, and Nicolas Courty. Semi-relaxed gromov-wasserstein divergence with applications on graphs. *arXiv preprint arXiv:2110.02753*, 2021.

[42] Anne K Voss and Andreas Strasser. The essentials of developmental apoptosis. *F1000Research*, 9, 2020.

[43] Xiaoyu Wei, Sulei Fu, Hanbo Li, Yang Liu, Shuai Wang, Weimin Feng, Yunzhi Yang, Xiawei Liu, Yan-Yun Zeng, Mengnan Cheng, et al. Single-cell stereo-seq reveals induced progenitor cells involved in axolotl brain regeneration. *Science*, 377(6610):eabp9444, 2022.

[44] Chen-Rui Xia, Zhi-Jie Cao, Xin-Ming Tu, and Ge Gao. Spatial-linked alignment tool (slat) for aligning heterogenous slices properly. *bioRxiv*, pages 2023–04, 2023.

[45] Ron Zeira, Max Land, Alexander Strzalkowski, and Benjamin J. Raphael. Alignment and integration of spatial transcriptomics data. *Nature Methods*, 19(5):567–575, may 2022.

Supplement

S1   Formulation

In vanilla optimal transport, and in the original formulation of `PASTE` [45], one has two constraints on alignment matrix $\mathbf{\Pi}$, given by probability measures $\mathbf{g}_1 \in \mathbb{R}^{n_1}, \mathbf{g}_2 \in \mathbb{R}^{n_2}$: the row-sum of $\mathbf{\Pi}$ must be $\mathbf{g}_1$, and the column-sum of $\mathbf{\Pi}$ must be $\mathbf{g}_2$. Measures $\mathbf{g}_1$ and $\mathbf{g}_2$ are supported on indices $i \in \{1, \ldots, n_1\}$ and $j' \in \{1, \ldots, n_2\}$, enumerating the spots of two slices of spatial transcriptomics data, $\mathcal{S}_1 = (\mathbf{X}^{(1)}, \mathbf{S}^{(1)})$ and $\mathcal{S}_1 = (\mathbf{X}^{(2)}, \mathbf{S}^{(2)})$. The rows $\mathbf{x}_i \equiv \mathbf{X}_{i,\cdot}^{(1)}$ of $\mathbf{X}^{(1)}$ and $\mathbf{x}'_{j'} \equiv \mathbf{X}_{j',\cdot}^{(2)}$ of $\mathbf{X}^{(2)}$ are indexed by spots, and each row is the expression vector at the given spot. Likewise, the rows $\mathbf{s}_i \equiv \mathbf{S}_{i,\cdot}^{(1)}$ of $\mathbf{S}^{(1)}$ and $\mathbf{s}'_{j'} \equiv \mathbf{S}_{j',\cdot}^{(2)}$ of $\mathbf{S}^{(2)}$ are the spatial coordinates of each spot. We use the convention that a prime on an index, e.g. j', refers to a spot in the second slice, while the absence of a prime on an index denotes a spot in the first slice.

S1.1   Context

In `PASTE`, a convex combination of standard inter-slice expression cost and a Gromov-Wasserstein cost are used (this combination referred to as *Fused Gromov-Wasserstein (FGW)*). The corresponding optimization problem is:

$$\min_{\mathbf{\Pi} \in \mathbb{R}_+^{n_1 \times n_2}} \quad \left\{ (1-\alpha) \sum_{i,j'} \mathbf{C}_{ij'} \mathbf{\Pi}_{ij'} + \alpha \sum_{i,j',k,l'} \left(\mathbf{D}_{ik}^{(1)} - \mathbf{D}_{j'l'}^{(2)} \right)^2 \mathbf{\Pi}_{ij'} \mathbf{\Pi}_{kl'} \right\}$$

$$s.t. \quad \mathbf{\Pi} \mathbf{1}_{n_2} = \mathbf{g}_1 = \frac{1}{n_1} \mathbf{1}_{n_1}, \quad \mathbf{\Pi}^T \mathbf{1}_{n_1} = \mathbf{g}_2 = \frac{1}{n_2} \mathbf{1}_{n_2}, \quad \mathbf{\Pi} \succcurlyeq 0 \tag{12}$$

Above, $\mathbf{C} \in \mathbb{R}^{n_1 \times n_2}$ is the inter-slice (gene expression) feature-distance matrix $\mathbf{C}_{ij'} \equiv \mathbf{C}(\mathbf{x}_i, \mathbf{x}'_{j'})$ whose ij'-th entry is the distance in expression space between the expression vector $\mathbf{x}_i$ at spot i in the first slice and the expression vector $\mathbf{x}'_{j'}$ at spot j' in the second slice. Matrices $\mathbf{D}^{(1)}$ and $\mathbf{D}^{(2)}$ in (12) are intra-slice (spatial) distance matrices. Define the 4-tensor $\mathbf{L} \equiv \mathbf{L}(\mathbf{D}^{(1)}, \mathbf{D}^{(2)}) \in \mathbb{R}^{n_1 \times n_2 \times n_1 \times n_2}$ entry-wise via

$$\mathbf{L}_{ij'kl'} := \left(\mathbf{D}_{ik}^{(1)} - \mathbf{D}_{j'l'}^{(2)} \right)^2 \tag{13}$$

We let $\otimes$ denote the tensor-matrix multiplication operator, such that for the alignment matrix $\mathbf{\Pi} \in \mathbb{R}_{\geq 0}^{n_1 \times n_2}$, $\mathbf{L} \otimes \mathbf{\Pi}$ denotes the $n_1 \times n_2$ matrix whose ij'-th entry is $\sum_{k,l'} \mathbf{L}_{ij'kl'} \mathbf{\Pi}_{kl'}$. Let $\langle \cdot, \cdot \rangle_F$ denote the Frobenius inner product of matrices. In this notation, the objective function (12) can be reformulated as follows:

$$\min_{\mathbf{\Pi} \in \mathbb{R}_+^{n_1 \times n_2}} \quad \left\{ (1-\alpha) \left\langle \mathbf{C}, \mathbf{\Pi} \right\rangle_F + \alpha \left\langle \mathbf{L} \otimes \mathbf{\Pi}, \mathbf{\Pi} \right\rangle_F \right\}$$

$$s.t. \quad \mathbf{\Pi} \mathbf{1}_{n_2} = \mathbf{g}_1 = \frac{1}{n_1} \mathbf{1}_{n_1}, \quad \mathbf{\Pi}^T \mathbf{1}_{n_1} = \mathbf{g}_2 = \frac{1}{n_2} \mathbf{1}_{n_2}, \quad \mathbf{\Pi} \succcurlyeq 0 \tag{14}$$

with $\mathbf{L}$ as in (13). The only difference between `PASTE2` [24] and the original `PASTE` is the inclusion of the constraint $\mathbf{1}_{n_1}^T \mathbf{\Pi} \mathbf{1}_{n_2} = s$, which goes along with a relaxation of the two marginal constraints to inequalities:

$$\min \quad (1-\alpha) \left\langle \mathbf{C}, \mathbf{\Pi} \right\rangle_F + \alpha \left\langle \mathbf{L} \otimes \mathbf{\Pi}, \mathbf{\Pi} \right\rangle_F$$

$$s.t. \quad \mathbf{\Pi} \mathbf{1}_{n_2} \leq \mathbf{g}_1 = \frac{1}{n_1} \mathbf{1}_{n_1}, \quad \mathbf{\Pi}^T \mathbf{1}_{n_1} \leq \mathbf{g}_2 = \frac{1}{n_2} \mathbf{1}_{n_2}, \quad \mathbf{1}_{n_1}^T \mathbf{\Pi} \mathbf{1}_{n_2} = s, \quad \mathbf{\Pi} \succcurlyeq 0$$

Note that by considering the dual problem, *partial optimal transport*, in which there is a constraint $s \in (0,1)$ on the total mass $\mathbf{1}_{n_1}^T \mathbf{\Pi} \mathbf{1}_{n_2}$ transported, can be seen as an instance of unbalanced optimal transport associated to the total variation φ-divergence (see [36] § 4.2). *Unbalanced optimal transport* refers to the version of (14) obtained by deleting the two hard constraints, $\mathbf{\Pi} \mathbf{1}_{n_2} = \mathbf{g}_1$ and $\mathbf{\Pi}^T \mathbf{1}_{n_1} = \mathbf{g}_2$, on the marginals of $\mathbf{\Pi}$, and instead adding to the cost function in brackets a pair of "soft constraints" in the form of two terms: $\mathrm{D}_\varphi(\mathbf{\Pi} \mathbf{1}_{n_2} | \mathbf{g}_1) + \mathrm{D}_\varphi(\mathbf{\Pi}^T \mathbf{1}_{n_1} | \mathbf{g}_2)$. Here, $\varphi : (0, \infty) \to [0, +\infty]$ is a so-called *entropy function*, namely it is convex, positive, lower-semi-continuous, and with $\varphi(1) = 0$. Let $\mathrm{D}_\varphi(\cdot | \cdot)$ denote the associated φ-divergence, defined for positive measures α, β on some common space $\mathcal{X}$ as $D_\varphi(\alpha | \beta) = \int_{\mathcal{X}} \varphi(\frac{\mathrm{d}\alpha}{\mathrm{d}\beta}) \mathrm{d}\beta$, where we have supposed α and β are mutually absolutely continuous, for instance. When $\varphi(p) = p \log p - p + 1$, one recovers the *Kullback-Leibler (KL) divergence*, which we denote by $\mathrm{D}_\varphi(\cdot | \cdot) = \mathrm{KL}(\cdot \| \cdot)$ in this case.

S1.2 `DeST-OT` objective

Our view of an OT objective function as a *Hamiltonian*, assigning an energy to a given transport plan $\mathbf{\Pi}$, motivates the terminology we use for its components below. The first change we address in the formulation of `DeST-OT`, relative to `PASTE`, is the constraints on the optimization together with our calibration of mass on the second slice. Specifically, we relax the constraint $\mathbf{\Pi}\mathbf{1}_{n_2} = \mathbf{g}_1$, while preserving the other. This fixes the total mass transported by $\mathbf{\Pi}$ to be the total mass of the second (usually larger, in the spatiotemporal setting) slice, which is equipped with positive, *not necessarily probability*, measure $\mathbf{g}_2 = \frac{1}{n_1}\mathbf{1}_{n_2}$. This allows the $\mathbf{\Pi}$-marginal over the first slice, namely $\mathbf{\Pi}\mathbf{1}_{n_2}$, to be non-uniform, while fixing its total mass to the value $\frac{n_2}{n_1}$. One is naturally lead to introduce a *mass-flux term*,

$$\boldsymbol{\xi} = \mathbf{\Pi}\mathbf{1}_{n_2} - \mathbf{g}_1, \tag{15}$$

as this object becomes non-zero as soon as we relax the first marginal constraint. In section S1.4, we discuss the value of $\boldsymbol{\xi}$. The non-uniformity in $\mathbf{\Pi}\mathbf{1}_{n_2}$ reflects that not all spots in the first slice are necessarily contributing the same amount to spots in the second slice – different cell types may have different growth rates.

The second change we address concerns the matrices used by the Gromov-Wasserstein (GW) term $\mathcal{E}_{\mathrm{GW}}(\mathbf{\Pi}) = \langle \mathbf{L} \otimes \mathbf{\Pi}, \mathbf{\Pi} \rangle$. This term favors $\mathbf{\Pi}$ matrices which are nearly isometries between the two slices, as whenever $\mathbf{D}^{(1)}_{ik} = \mathbf{D}^{(2)}_{j'l'}$, the corresponding summand of the GW term $\mathcal{E}_{\mathrm{GW}}(\mathbf{\Pi})$ vanishes. For a more general pair of intra-slice cost matrices, (symmetric, non-negative matrices) $\mathbf{M}^{(1)} \in \mathbb{R}^{n_1 \times n_1}$ and $\mathbf{M}^{(2)} \in \mathbb{R}^{n_2 \times n_2}$, we generalize (13), defining the 4-tensor $\mathbf{L}^{\mathbf{M}} \equiv \mathbf{L}^{\mathbf{M}}(\mathbf{M}^{(1)}, \mathbf{M}^{(2)}) \in \mathbb{R}^{n_1 \times n_2 \times n_1 \times n_2}$ entry-wise via

$$\mathbf{L}^{\mathbf{M}}_{i\,j'\,k\,l'} := \left(\mathbf{M}^{(1)}_{ik} - \mathbf{M}^{(2)}_{j'l'} \right)^2, \tag{16}$$

and we define the analogous GW energy (using $\mathbf{M}^{(i)}$ in place of the $\mathbf{D}^{(i)}$). We also refer to it as a *quartet* energy, as each summand defining it corresponds to two pairs points:

$$\mathcal{E}^{\mathbf{M}}_{\mathrm{GW}}(\mathbf{\Pi}) \equiv \mathcal{E}^{\mathbf{M}}_{\mathrm{quartet}}(\mathbf{\Pi}) = \langle \mathbf{L}^{\mathbf{M}} \otimes \mathbf{\Pi}, \mathbf{\Pi} \rangle. \tag{17}$$

We define the matrices $\mathbf{M}^{(i)}$ from a pair of expression distance matrices for the first and second slice, $\mathbf{C}^{(1)} \in \mathbb{R}^{n_1 \times n_1}$, $\mathbf{C}^{(2)} \in \mathbb{R}^{n_2 \times n_2}$. These intra-slice feature matrices $\mathbf{C}^{(i)}$ are distinct from their inter-slice counterpart $\mathbf{C} \in \mathbb{R}^{n_1 \times n_2}_{+}$ which contains the distance in (expression) feature space from spots in slice 1 and slice 2, and is therefore not a symmetric, square matrix in general. We specifically choose $\mathbf{M}^{(i)}$ to be the Hadamard product of matrices $\mathbf{C}^{(i)}$ and $\mathbf{D}^{(i)}$, so that entry-wise, one defines $\mathbf{M}^{(1)}_{ik} = \mathbf{C}^{(1)}_{ik}\mathbf{D}^{(1)}_{ik}$ and $\mathbf{M}^{(2)}_{j'l'} = \mathbf{C}^{(2)}_{j'l'}\mathbf{D}^{(2)}_{j'l'}$. We refer to the $\mathbf{M}^{(i)}$ as *merged feature-spatial matrices*.

To $\mathcal{E}^{\mathbf{M}}_{\mathrm{GW}}$, we add a symmetric pair of terms $\mathcal{E}^{\mathbf{M}}_{\mathrm{triplet}(1)}$ and $\mathcal{E}^{\mathbf{M}}_{\mathrm{triplet}(2)}$ of the form

$$\begin{aligned} \mathcal{E}^{\mathbf{M}}_{\mathrm{triplet}(1)}(\mathbf{\Pi}) &= \mathrm{Tr}\left[\mathbf{\Pi}\mathbf{V}^{(2)}\mathbf{\Pi}^T \right] = \sum_{i,j',k'} \mathbf{\Pi}_{ij'}\mathbf{\Pi}_{ik'}\mathbf{V}^{(2)}_{j'k'}, \\ \mathcal{E}^{\mathbf{M}}_{\mathrm{triplet}(2)}(\mathbf{\Pi}) &= \mathrm{Tr}\left[\mathbf{\Pi}^T\mathbf{V}^{(1)}\mathbf{\Pi} \right] = \sum_{i,j,k'} \mathbf{\Pi}_{ik'}\mathbf{\Pi}_{jk'}\mathbf{V}^{(1)}_{ij} \end{aligned} \tag{18}$$

When $\mathbf{V}^{(2)} = (\mathbf{M}^{(2)})^2$, i.e. entry-wise squaring of the merged feature-spatial matrix, which is why the superscript indicates the same dependence on the $\mathbf{M}$-matrices as the GW term. Note that $\mathcal{E}^{\mathbf{M}}_{\mathrm{triplet}(1)}$ is identical to the terms in the sum defining $\mathcal{E}^{\mathbf{M}}_{\mathrm{GW}}$ which have $i = k$, which is why we name it for the first slice instead using the index of the merged feature-spatial matrix involved in the definition. This energy $\mathcal{E}^{\mathbf{M}}_{\mathrm{triplet}(1)}$ favors $\mathbf{\Pi}$ which predict a localized (in space, and in gene expression space) set of possible ancestors for each spot in the second slice.

Likewise, when $\mathbf{V}^{(1)} = (\mathbf{M}^{(1)})^2$, energy $\mathcal{E}^{\mathbf{M}}_{\mathrm{triplet}(2)}$ is identical to the terms in the sum defining $\mathcal{E}^{\mathbf{M}}_{\mathrm{GW}}$ for which $j' = \ell'$, and so is named for the second slice. Transport plans $\mathbf{\Pi}$ with low $\mathcal{E}^{\mathbf{M}}_{\mathrm{triplet}(2)}$-energy are more likely to predict that descendants of a given spot in the first slice are close (spatially, and in feature-distance) in the second slice. Together, $\mathcal{E}^{\mathbf{M}}_{\mathrm{triplet}(1)}$ and $\mathcal{E}^{\mathbf{M}}_{\mathrm{triplet}(2)}$ encourage spot-wise continuity in $\mathbf{\Pi}$, without penalizing $\mathbf{\Pi}$ for spatial distortions intrinsic to tissue growth, or for change in expression characteristic of development. We refer to the sum of these terms as the *triplet* energy between triplets of points, $\mathcal{E}_{\mathrm{triplet}}$:

$$\mathcal{E}^{\mathbf{M}}_{\mathrm{triplet}}(\mathbf{\Pi}) = \mathcal{E}^{\mathbf{M}}_{\mathrm{triplet}(1)}(\mathbf{\Pi}) + \mathcal{E}^{\mathbf{M}}_{\mathrm{triplet}(2)}(\mathbf{\Pi}) \tag{19}$$

14

Combining these changes, and adding in a term of entropy regularization, the formulation [1] used by `DeST-OT` is:

$$\min \quad (1-\alpha)\underbrace{\left\langle \mathbf{C}, \mathbf{\Pi} \right\rangle_F}_{\mathcal{E}_{\text{doublet}}(\mathbf{\Pi})} + \frac{\alpha}{2}\left(\mathcal{E}^{\mathbf{M}}_{\text{triplet}}(\mathbf{\Pi}) + \mathcal{E}^{\mathbf{M}}_{\text{quartet}}(\mathbf{\Pi}) \right) + \gamma\text{KL}(\mathbf{\Pi}\mathbf{1}_{n_2} \parallel \mathbf{g}_1) - \epsilon\text{H}(\mathbf{\Pi}) \tag{20}$$

$$s.t. \quad \mathbf{\Pi}^T\mathbf{1}_{n_1} = \mathbf{g}_2 = \frac{1}{n_1}\mathbf{1}_{n_2}, \quad \mathbf{g}_1 = \frac{1}{n_1}\mathbf{1}_{n_1}, \quad \mathbf{\Pi} \succcurlyeq 0$$

with $\mathbf{L^M}$ defined in (16), and the notation $\mathbf{L^M} \otimes \mathbf{\Pi}$ as defined just below (13). The choices of $\mathbf{V}^{(1)} = ((\mathbf{M}^{(1)})^2$ and $\mathbf{V}^{(2)} = ((\mathbf{M}^{(2)})^2$ as above enable us to write the sum of our triplet and quartet energies in (20) as

$$\left\langle \widetilde{\mathbf{L}}^{\mathbf{M}} \otimes \mathbf{\Pi}, \mathbf{\Pi} \right\rangle = \sum_{ij'kl'} (1 + \delta_{ik} + \delta_{j'l'})\left(\mathbf{M}^{(1)}_{ik} - \mathbf{M}^{(2)}_{j'l'} \right)^2 \mathbf{\Pi}_{ij'}\mathbf{\Pi}_{kl'} \tag{21}$$

where δ_{ik} is 1 if and only if $i = k$ and is 0 otherwise. The 4-tensor $\widetilde{\mathbf{L}}^{\mathbf{M}}$ is defined implicitly by the above display, and the objective function used by `DeST-OT` can now expressed concisely as follows, though (20) is the expression we use in practice for computing gradients:

$$(1-\alpha)\left\langle \mathbf{C}, \mathbf{\Pi} \right\rangle_F + \frac{\alpha}{2}\underbrace{\left\langle \widetilde{\mathbf{L}}^{\mathbf{M}} \otimes \mathbf{\Pi}, \mathbf{\Pi} \right\rangle_F}_{\mathcal{E}^{\mathbf{M}}(\mathbf{\Pi})} + \gamma\text{KL}(\mathbf{\Pi}\mathbf{1}_{n_2} \parallel \mathbf{g}_1) - \epsilon\text{H}(\mathbf{\Pi}) \tag{22}$$

As indicated by the underbrace in (22), we define the *merged feature-spatial energy*, denoted $\mathcal{E}^{\mathbf{M}}(\mathbf{\Pi})$ to be the sum of $\mathcal{E}^{\mathbf{M}}_{\text{quartet}}(\mathbf{\Pi})$ and $\mathcal{E}^{\mathbf{M}}_{\text{triplet}}(\mathbf{\Pi})$, to have a more descriptive way of referring to the left-hand side of (21).

S1.3 Connection to energy-based models

Owing to the presence of multiple energetic conditions, including within-slice energies and matching energies, we make a connection between the optimal transport problem we have defined and an energy-based model. For some energy function $\mathcal{E}_\theta(\boldsymbol{x}) \geq 0$, and for some variable we are optimizing $\boldsymbol{x}(\triangleq \mathbf{\Pi}$ in our case), one may define a Gibbs-Boltzmann distribution $P_\theta(\boldsymbol{x})$ given by:

$$P_\theta(\boldsymbol{x}) = \frac{1}{Z_\theta}e^{-\mathcal{E}_\theta(\boldsymbol{x})},$$

where θ comes from the SRT data, $\theta = (\mathbf{C}, \mathbf{C}^{(1)}, \mathbf{C}^{(2)}, \mathbf{X}^{(1)}, \mathbf{X}^{(2)})$. The normalizing constant (or *partition function*) Z_θ is given by $Z_\theta = \int_{\boldsymbol{x}} e^{-\mathcal{E}_\theta(\boldsymbol{x})}\mathrm{d}\boldsymbol{x}$, which is generally intractable to compute. For such an energy-based model, in order to find an optimal value for $\boldsymbol{x}$, one may optimize the the log-likelihood of the model given by $\nabla_{\boldsymbol{x}}\log P_\theta(\boldsymbol{x})$, where:

$$\nabla_{\boldsymbol{x}}\log P_\theta(\boldsymbol{x}) = \nabla_{\boldsymbol{x}}\left(-\mathcal{E}_\theta(\boldsymbol{x}) - \int_{\boldsymbol{x}} e^{-\mathcal{E}_\theta(\boldsymbol{x})}d\boldsymbol{x} \right) = -\nabla_{\boldsymbol{x}}\mathcal{E}_\theta(\boldsymbol{x})$$

which holds as the partition function is clearly a constant with respect to $\boldsymbol{x}$. For the Wasserstein energy $\langle \mathbf{C}, \boldsymbol{x} \rangle$, if $\mathcal{E}_\theta(\boldsymbol{x}) = -\langle \mathbf{C}, \boldsymbol{x} \rangle_F$ represents our energy function, we are simply solving a standard optimal-transport problem. If $\mathcal{E}_\theta(\boldsymbol{x}) = -((1-\alpha)\langle \boldsymbol{C}, \boldsymbol{x} \rangle_F + \alpha\langle \mathbf{L^D} \otimes \mathbf{\Pi}, \mathbf{\Pi} \rangle_F)$, then we are solving an FGW optimal-transport problem, and so on. While the connection to energy-functions is trivially evident, the value of introducing the connection is seen in the product-of-experts formulation of energy-based models, where one may have multiple Gibbs-Boltzmann distributions $P_\theta^{(1)}, P_\theta^{(2)}, ..., P_\theta^{(N)}$, each carrying some "expert" information, where the distribution representing the combination of the features of all of the distributions is called a product-of-experts [16], given by:

$$P_\theta(\boldsymbol{x}) = \frac{1}{Z_\theta^{(1:N)}}\prod_{i=1}^{N} P_\theta^{(i)}(\boldsymbol{x}) = \frac{1}{Z_\theta^{(1:N)}}\prod_{i=1}^{N}\frac{1}{Z_\theta^{(i)}}e^{-\mathcal{E}_\theta^{(i)}(\boldsymbol{x})} \propto_{\boldsymbol{x}} e^{-\sum_{i=1}^{N}\mathcal{E}_\theta^{(i)}(\boldsymbol{x})}$$

Where the energy-function of the final Gibbs-Boltzmann distribution is given by the *sum* of the individual energies:

$$\mathcal{E}_\theta(\boldsymbol{x}) = \mathcal{E}_\theta^{(1)}(\boldsymbol{x}) + ... + \mathcal{E}_\theta^{(i)}(\boldsymbol{x}) + ... + \mathcal{E}_\theta^{(N)}(\boldsymbol{x})$$

---

[1]All matrices involved are subject to a consistent data-dependent normalization by matrix norms which ensure the terms of the gradient are scaled analogously, such that $\alpha = 0.5$ roughly means both terms contribute equal weight for interpretability and robustness of the hyper-parameter defaults to different datasets.

15

As such, we augment the optimal-transport formulation by framing it as a product-of-experts, constructing a total-energy which we optimize with respect to $\mathbf{\Pi}$ that carries the standard Wasserstein (doublet) energy $\langle \mathbf{C}, \mathbf{\Pi} \rangle_F$, the quartet energy $\langle \mathbf{L^M} \otimes \mathbf{\Pi}, \mathbf{\Pi} \rangle_F$ defined through the merged feature-spatial matrices, and two triplet energies which are also defined from these matrices: $\mathrm{Tr}\left[\mathbf{\Pi M}^{(2)}\mathbf{\Pi}^T\right]$ and $\mathrm{Tr}\left[\mathbf{\Pi}^T\mathbf{M}^{(1)}\mathbf{\Pi}\right]$. Denoting the optimal-transport entropic-term density $P_{\mathcal{H}}$, we minimize the following product-of-experts Gibbs-Boltzmann distribution with respect to $\mathbf{\Pi}$:

$$P_\theta(\mathbf{\Pi}) = \frac{1}{Z_\theta} P_{\mathcal{H}}(\mathbf{\Pi}) \times e^{-\mathcal{E}_{\mathrm{expression}}(\mathbf{\Pi})} \times e^{-\mathcal{E}_{\mathrm{GW}}(\mathbf{\Pi})} \times e^{-\mathcal{E}_{\mathrm{triplet}(1)}(\mathbf{\Pi})} \times e^{-\mathcal{E}_{\mathrm{triplet}(2)}(\mathbf{\Pi})}$$

$$= \frac{1}{Z_\theta} P_{\mathcal{H}}(\mathbf{\Pi}) \times \exp\left\{ \langle \mathbf{C}, \mathbf{\Pi} \rangle_F + \langle \mathbf{L^M} \otimes \mathbf{\Pi}, \mathbf{\Pi} \rangle_F + \mathrm{Tr}\left[\mathbf{\Pi}^T\mathbf{M}^{(1)}\mathbf{\Pi}\right] + \mathrm{Tr}\left[\mathbf{\Pi M}^{(2)}\mathbf{\Pi}^T\right] \right\}$$

Which offers the interpretation that taking the sum of the energy terms in our optimal-transport problem is equivalent to optimizing a product of the Boltzmann-distributions over our variable $\mathbf{\Pi}$, where this product represents a product-of-experts in which each "expert" distribution refines the matrix $\mathbf{\Pi}$ to be more biologically and spatially realistic with respect to the transcriptomic and spatial geometry of the first and second slices. Alternatively viewing each term as representing pairwise motifs (Wasserstein, or *doublet* term), ternary motifs (*triplet* term), and quaternary motifs (GW, or *quartet* term), these experts capture features ranging from lower to higher order.

S1.4 On the mass-flux term, semi-relaxed OT

The semi-relaxed approach has been explicitly discussed in [41, 12, 6, 4, 32, 7]. Blondel et al. [4] formulate a version of our problem in their Definition 3 ("semi-relaxed smooth primal"), fixing their second marginal as we do, but without using entropic regularization in order to produce sparse transport plans. These authors point out that the mixed relaxed distance introduced by Benamou in [2] is a version of semi-relaxed OT, fixing the first marginal instead of a second, and using an ℓ^2-penalty in place of a KL penalty. Interestingly, this penalty is applied directly to the analogue of ξ in this setting. A recent paper of Dong et al. [12] uses semi-relaxed transport for domain adaptation, aligning imaging data of different modalities. These authors use a Wasserstein loss, fixing the first marginal and in addition constraining the total mass transported. Vincent-Cuaz et al. [41] apply the semi-relaxed framework to graph matching, fixing the first marginal, and using a GW loss function. For matching two graphs, they find that fixing the first marginal while relaxing the second better preserves the structure of the first graph under the transport plan, versus the balanced regime. These authors [41] note that semi-relaxed OT (in the absence of entropy regularization) produces sparser transport plans than vanilla optimal transport. This sparsity also motivated the earlier work of [32] on color transfer; maps that are "too" multi-valued (i.e. not sparse enough) can inappropriately mix colors being transferred and create spatial irregularities. These authors also fix the first marginal, using a sparse transport plan to assign colors from the second image to the pixel of the first, while preserving its geometry. On the theoretical side, Chizat et al. [7] introduce the notion of a semi-coupling to connect the (PDE) dynamic and static pictures of semi-relaxed OT. Lastly, we mention two studies of Frank-Wolfe [13] and Sinkhorn [14] in the semi-relaxed setting.

We now discuss some properties of the mass-flux term ξ built from $\mathbf{\Pi}$ and advantages our formulation give us. Let us start by examining the objects analogous to ξ in the fully-unbalanced case. When both marginal constraints are relaxed, both of the vectors $\xi_1 = \mathbf{\Pi 1}_{n_2} - \mathbf{g}_1$ and $\xi_2 = \mathbf{\Pi}^T\mathbf{1}_{n_1} - \mathbf{g}_2$ may be non-zero. Towards relating vectors ξ_1 and ξ_2, we take the inner product of these expressions with $\mathbf{1}_{n_i}$ to obtain:

$$\mathbf{1}_{n_1}^T \xi_1 = \mathbf{1}_{n_1}^T \mathbf{\Pi 1}_{n_2} - \mathbf{1}_{n_1}^T \mathbf{g}_1 \quad \text{and} \quad \mathbf{1}_{n_2}^T \xi_2 = \mathbf{1}_{n_2}^T \mathbf{\Pi}^T \mathbf{1}_{n_1} - \mathbf{1}_{n_2} \mathbf{g}_2,$$

We solve each of these for the total mass transported, namely $\mathbf{1}_{n_1}^T \mathbf{\Pi 1}_{n_2} \equiv \mathbf{1}_{n_2}^T \mathbf{\Pi}^T \mathbf{1}_{n_1}$. After relating the two expressions through the total mass transported and re-arranging terms, one has

$$\mathbf{1}_{n_1}^T \xi_1 - \mathbf{1}_{n_2}^T \xi_2 = \mathbf{1}_{n_2}^T \mathbf{g}_2 - \mathbf{1}_{n_1}^T \mathbf{g}_1$$
$$\equiv \frac{n_2 - n_1}{n_1},$$

with the last line following from our choice of normalization on the uniform measures $\mathbf{g}_1 = \frac{1}{n_1}\mathbf{1}_{n_1}$ and $\mathbf{g}_2 = \frac{1}{n_1}\mathbf{1}_{n_2}$.

In the semi-relaxed context of DeST-OT, $\xi \equiv \xi_1$, and vector ξ_2 is zero, in which case, one has

$$\mathbf{1}_{n_1}^T \xi = \frac{n_2 - n_1}{n_1}.$$

16

Thus, the semi-relaxed formulation allows us to describe all growth and death implicit in transport plan $\mathbf{\Pi}$ by a single vector $\boldsymbol{\xi}$, instead of a pair of vectors $(\boldsymbol{\xi}_1, \boldsymbol{\xi}_2)$ of different dimensionality. Moreover, the hard constraint of the semi-relaxed formulation makes this single vector $\boldsymbol{\xi}$ interpretable in a way that the pair $(\boldsymbol{\xi}_1, \boldsymbol{\xi}_2)$ is not. Observe that the second marginal $\mathbf{g}_2$ is fixed, with units assigning mass $\frac{1}{n_1}$ to each spot. Though the first marginal of $\mathbf{\Pi}$ is no longer fixed, $\boldsymbol{\xi}$ is by definition an additive perturbation of $\mathbf{g}_1$ which uses the same units as $\mathbf{g}_2$, also assigning mass $\frac{1}{n_1}$ to each spot. $\boldsymbol{\xi}$ also uses these units, giving expression $\mathbf{g}_1 + \boldsymbol{\xi}$ physical meaning.

Rescaled vector $\mathbf{q}_1 = n_1(\mathbf{\Pi} \mathbf{1}_{n_2})$ has in its i-th element the amount of mass transported from spot i, in units of *numbers of spots*. These numbers are fractional, as $\mathbf{\Pi}$ is implicitly estimating these values in a sense averaged over $t_2 - t_1$, with respect to a stochastic process similar to the one described in [6]. Because the rescaled target measure $n_1 \mathbf{g}_2$ shares these counting-measure units, we can reasonably interpret $\mathbf{q}_1 \equiv \mathbf{q}_1(\mathbf{\Pi})$ as the vector of the *expected number of descendants* of each spot in the first slice, as predicted by $\mathbf{\Pi}$. This is clear, as we have:

$$\mathbb{E}_{\sim \mathcal{S}_1, \mathcal{S}_2}[\sum_{j \in \mathcal{S}_2} \mathbb{1}[i \to j]] = \sum_{j \in \mathcal{S}_2} \mathbb{E}_{\sim \mathcal{S}_1, \mathcal{S}_2}[\mathbb{1}[i \to j]] = \sum_{j \in \mathcal{S}_2} \mathbf{\Pi}_{i,j} \triangleq \mathbf{q}_{1,i}/n_1$$

Where multiplying by n_1 scales $\mathbf{q}_1$ to have the units of counting measure over spots. We lose this interpretation in the fully-unbalanced regime: when the target measure is not constrained to be uniform, the amount of mass transported *from* spot i may not reflect an expected number of descendants, as this value will depend on the mass of each descendant.

From the definitions of $\boldsymbol{\xi}$ and $\mathbf{q}_1$, we have

$$n_1 \boldsymbol{\xi} = \mathbf{q}_1 - \mathbf{1}_{n_1},$$

and $n_1 \boldsymbol{\xi}$ has the following intuitive interpretation: at spot i,

$$n_1 \boldsymbol{\xi}_i = \text{Expected number of \textbf{branches/descendants} contributed from spot i}$$

S2 Growth rate conversion

The conversion of the growth vector (mass-flux) $\boldsymbol{\xi}$ to a growth rate can be done simply. We use the growth process described in [22], where one considers the PDE modeling a transcriptomic trajectory as a density evolving in time:

$$\frac{\partial \rho}{\partial t} = -\boldsymbol{\nabla} \cdot (\rho \mathbf{F}) + \frac{\sigma^2}{2} \Delta \rho + J\rho$$

With $-\boldsymbol{\nabla} \cdot (\rho \mathbf{F})$ a continuity equation drift term, $\frac{\sigma^2}{2} \Delta \rho$ a diffusion term, and $J\rho$ a term representing growth and branching, which are all modeled using successive optimal transport steps. We convert our mass-flux term from the optimal transport to a growth using the principle of [22], where operator-splitting the branching component above from the drift-diffusion gives us a continuous-time growth update as:

$$\partial_t \rho = J\rho$$

Thus we simply need to consider the solution to the ordinary differential equation $\dot{\rho} = J\rho$ for J between times t_1, t_2:

$$\rho(t_2) = e^{J(t_2 - t_1)} \rho(t_1)$$

For $\rho(t_1)$ and $\rho(t_2)$ a prior and posterior density over the spots in the first slice. By the semi-relaxed optimal transport formulation, we simply compare against a simple uniform prior density $\rho(t_1) = \frac{1}{n_1}$ which we start with. Thus one concludes the connection to a growth rate, on a per-spot basis in the first slice, is given as:

$$J = \frac{\log (\rho(t_2) n_1)}{t_2 - t_1} = \frac{\log (n_1 \xi + 1)}{t_2 - t_1}$$

Which establishes a simple monotonic connection between our growth vector $\boldsymbol{\xi}$ and a proper growth rate in time. In the notation of [22], $\tau = t_2 - t_1$, and one has $J = \tau^{-1}(p_b - p_d)$, establishing a connection between the growth rate and birth-death parameters p_b, p_d, and τ. Conventionally, cell division and death are modeled as follows: each cell has an exponential clock of rate τ^{-1}. When a cell's clock rings, it dies with probability p_d, or splits into two cells with probability $p_b = 1 - p_d$. As such, our growth rates have a natural connection to the parameters of this birth-death process.

S3 Connection to the continuity equation and interpretation of growth vector

Suppose we denote $\mathbf{x}(t_k) = \mathbf{x} \sim \mu$, $\mathbf{x}(t_{k+1}) = \mathbf{y} \sim \nu$ as samples of our slices $\mathcal{S}_1$ and $\mathcal{S}_2$, and consider the pairwise-alignment problem in the equivalent Monge-formulation (the discrete analogue of μ being $\mathbf{g_1}$, and ν being $\mathbf{g_2}$). The Monge-problem is formulated as:

$$\inf_{\mathbf{T}:\mathbf{T}\#\mu=\nu} \int_{\mathbb{R}^d} \|\mathbf{T}(\mathbf{x}) - \mathbf{x}\|_2 d\mu(\mathbf{x})$$

Where it can be shown that an equivalent form exists in which the transport-map can be expressed as the integral of some vector field $\mathbf{F}(\mathbf{x}, t)$, weighted by a time-dependent density $\rho(\mathbf{x}, t)$ and where the optimization is performed over a vector-field of least-norm:

$$\mathcal{W}_2^2(\mu, \nu) = \inf_{(\rho, \mathbf{F})} \quad T \int_{\mathbb{R}^d} \int_0^T \rho(\mathbf{x}, t) \|\mathbf{F}(\mathbf{x}, t)\|_2^2 d\mathbf{x} dt$$
$$\text{s.t.} \quad \rho(\cdot, t_k) = \mu$$
$$\rho(\cdot, t_{k+1}) = \nu$$

(23)

Where the vector field is optimized subject to the continuity equation: $\partial_t \rho = -\boldsymbol{\nabla} \cdot (\rho \mathbf{F}(\mathbf{x}, t))$ [39]. In the semi-relaxed case, one may either assume mass-conservation or generalize the vanilla continuity equation by assuming the presence of a source or sink term σ (i.e. $\sigma = J\rho$ for J a growth rate as defined in S2) which allows mass to be introduced into the system in the form $\partial_t \rho = -\boldsymbol{\nabla} \cdot (\rho \mathbf{F}(\mathbf{x}, t)) + J\rho$. As such, $\boldsymbol{\xi}$ represents the integral of a divergence in the case of mass-conservation (i.e. local mass-redistribution), or a spatial divergence added to a source/sink term in the case where the total mass is increased or decreased in the system. To be precise, we have that in the balanced case:

$$\boldsymbol{\xi}(\mathbf{x}) = \int_{t_1}^{t_2} \left(\frac{\partial \rho}{\partial t}\right) dt = \int_{t_1}^{t_2} -\boldsymbol{\nabla} \cdot (\rho \mathbf{F}(\mathbf{x}, t)) \, dt$$

And general semi-relaxed case:

$$\boldsymbol{\xi}(\mathbf{x}) = \int_{t_1}^{t_2} \left(\frac{\partial \rho}{\partial t}\right) dt = \int_{t_1}^{t_2} (-\boldsymbol{\nabla} \cdot \rho \mathbf{F}(\mathbf{x}, t) + \sigma) \, dt$$

S3.1 Interpretation of ξ

Supposing we call the spatial volume encompassed by our tissue slice at time t, V_t. Each element of ξ, ξ_k, represents the approximate value of $\boldsymbol{\nabla} \cdot (\rho(x_k, y_k) \mathbf{F}(\mathbf{x}, t)(x_k, y_k))$ in some box $[x_k - \Delta, x_k + \Delta] \times [y_k - \Delta, y_k + \Delta]$ centered at $(x_k, y_k) \in V_t$. Generally speaking the volume V_t is assumed to be connected such that, for N_t dots at time t, the volume is $V_t = \cup_{k=1}^{N_t} [x_k - \Delta, x_k + \Delta] \times [y_k - \Delta, y_k + \Delta]$.

We assume a cell type assignment is some function from a matrix of distance-based dissimilarities and feature-values to a partition $\mathcal{P}$ of the data $\phi(D, C) = \mathcal{P}$. Where $\mathcal{P} = \{\mathcal{P}_k\}_{k=1}^K$ represents a decomposition of our dots into disjoint sets representing respective cell types. Following from this, we define the volume of a cell type k at time t, $V_{t,k}$, as $V_{t,k} = \cup_{(x_i, y_i) \in \mathcal{P}_k} [x_i - \Delta, x_i + \Delta] \times [y_i - \Delta, y_i + \Delta]$. Clearly, $V_t = \cup_{k=1}^K V_{t,k}$.

Definition 1. *Tissue-slice growth. The term* $\mathbf{1}^T \boldsymbol{\xi} = \sum_x \sum_y \int_{t_1}^{t_2} -\boldsymbol{\nabla} \cdot (\rho(x, y) \mathbf{F}(\mathbf{x}, t)(x, y))$ *represents the discretized volume integral*

$$\int_{t_1}^{t_2} \iint_{V_t} -\boldsymbol{\nabla} \cdot (\rho(x, y) \mathbf{F}(\mathbf{x}, t)(x, y)) \, dV_t = -\int_{t_1}^{t_2} \oint_{\partial V_t = S_t} (\rho \mathbf{F}(\mathbf{x}, t)) \cdot \hat{n} dS_t$$

for $\Delta = 1/2$. By the divergence theorem, one identifies the sum of the divergences in the volume V_t as the mass-flux across the boundary ∂V_t. Thus, the growth of a tissue slice contained within in a volume at time t, V_t, is defined as the mass-flux across this boundary integrated from t_1 to t_2.

For a balanced optimal transport this is identically zero for any boundary as $\boldsymbol{\xi} = \mathbf{0}$:

$$\mathbf{1}_{n_1}^T \boldsymbol{\xi} = \mathbf{1}_{n_1}^T (\boldsymbol{\Pi} \mathbf{1}_{n_2} - \mathbf{g_1}) = \mathbf{1}_{n_1}^T \mathbf{0}_{n_1} = 0$$

18

For a semi-relaxed optimal transport with marginals that sum to the same value, such as the uniform marginals $\Pi^{\mathbf{T}}\mathbf{1}_{n_1} = \mathbf{g}_2 = \frac{1}{n_2}\mathbf{1}_{n_2}$ and marginal $\mathbf{g}_1 = \frac{1}{n_1}\mathbf{1}_{n_1}$, one may have *local* growth or death as $\boldsymbol{\xi}$ is not necessarily the zero-vector, but globally mass is conserved:

$$\mathbf{1}_{n_1}^T\boldsymbol{\xi} = \left(\Pi^{\mathbf{T}}\mathbf{1}_{n_1}\right)^{\mathbf{T}}\mathbf{1}_{n_2} - \mathbf{1}_{n_1}^T\mathbf{g}_1 = \mathbf{g}_2^T\mathbf{1}_{n_2} - \mathbf{1}_{n_2}^T\mathbf{g}_1 = 0$$

In the case of a semi-relaxed optimal transport, if we allow for this source or sink term where

$$\mathbf{1}^T\boldsymbol{\xi} = \int_{t_1}^{t_2}\oint_{\partial V_t = S_t}\left(-\rho\mathbf{F}(\mathbf{x},t) + \sigma\right)\cdot\hat{n}dS_t$$

we generalize the above definition by asserting global mass gain or loss is possible. In particular, we can set the unbalanced marginals to reflect the normalized change in volume (or change in mass) as:

$$\mathbf{1}_{n_1}^T\boldsymbol{\xi} = \mathbf{g}_2^T\mathbf{1}_{n_2} - \mathbf{1}_{n_1}^T\mathbf{g}_1 = \eta \tag{24}$$

Where $\eta \in \mathbb{R}$ could be chosen to reflect something known–such as a total change of mass or volume between the two slices. We also note that the interpretation of $\boldsymbol{\xi}$ can also be used to measure local growth of a tissue within some fixed boundary, as described in the corollary below.

Corollary 1 (Cell type growth). *Given a partition $\mathcal{P}$ of tissue into separate cell types, and defining the vector $\mathbf{z}_p$ by*

$$(\mathbf{z}_p)_k = \begin{cases} 1 \text{ if } (x_k, y_k) \in \mathcal{P}_p \\ 0 \text{ otherwise} \end{cases}$$

The term $\mathbf{z}_p^T\boldsymbol{\xi}$ represents the volume integral

$$\int_{t_1}^{t_2}\iint_{V_{t,p}} -\boldsymbol{\nabla}\cdot(\rho(x,y)\mathbf{F}(\mathbf{x},t)(x,y))\,dV_{t,p} = -\int_{t_1}^{t_2}\oint_{\partial V_{t,p}=S_{t,p}}(\rho\mathbf{F}(\mathbf{x},t))\cdot\hat{n}dS_{t,p}$$

and represents the mass-flux out of the boundary of cell type p, $\partial V_{t,p}$, integrated from t_1 to t_2.

S3.2   Defining an Unbalanced Optimal Transport problem to match an a priori known total mass-flux

We seek a balancing condition which fixes the mass-flux η from our optimal transport 24 to some interpretable and meaningful value. By our previous decomposition of the volume of a bar-coded grid of spots into boxes of equal volume Δ^2, or analogously a small hexagonal volume for Visium, and our assumption that the mass-density is constant for each spot, we have that the normalized mass-flux above must equate to:

$$= \frac{\int_{\mathcal{S}_2}\rho_M(\mathbf{x}_2)dV(\mathbf{x}_2) - \int_{\mathcal{S}_1}\rho_M(\mathbf{x}_1)dV(\mathbf{x}_1)}{\int_{\mathcal{S}_1}\rho_M(\mathbf{x}_1)dV(\mathbf{x}_1)} = \frac{\int_{\mathcal{S}_2}dV(\mathbf{x}_2) - \int_{\mathcal{S}_1}dV(\mathbf{x}_1)}{\int_{\mathcal{S}_1}dV(\mathbf{x}_1)} \triangleq \frac{1}{|\mathbf{vol}\left(\mathcal{S}_1\right)|}\int_{t_1}^{t_2}\left(\frac{\partial\mathbf{vol}S}{\partial t}\right)dt,$$

as we assume that the mass-density $\rho_M(\mathbf{x}) = C$ is constant for any spot on the grid.

For Δ^2 a per-spot volume, we see that the volume-normalization lets this technology-specific factor cancel and the sum of the growth $\boldsymbol{\xi}$ is related to the change-in-spots directly as

$$\mathbf{1}_{n_1}^T\boldsymbol{\xi} = \frac{|\mathbf{vol}\left(\mathcal{S}_2\right)| - |\mathbf{vol}\left(\mathcal{S}_1\right)|}{|\mathbf{vol}\left(\mathcal{S}_1\right)|} = \frac{\Delta^2(n_2 - n_1)}{\Delta^2 n_1} = \frac{n_2 - n_1}{n_1}$$

Which requires that the unbalanced condition have $\mathbf{g}_2 = \frac{1}{n_1}\mathbf{1}_{n_2}$ as the constraint measure. This makes sense, as $\mathbf{1}_{n_1}^T\mathbf{g}_1 = \mathbf{1}_{n_1}^T\mathbf{1}_{n_1}\frac{1}{n_1} = 1$ and $\mathbf{1}_{n_2}^T\mathbf{g}_2 = \mathbf{1}_{n_2}^T\mathbf{1}_{n_2}\frac{1}{n_1} = \frac{n_2}{n_1}$, which has the interpretation that the density in the first slice sums to 1, and the density of the second is proportional to the ratio of the number of spots of the second slice to the first. With $\frac{n_2}{n_1} > 1$ implying mass is generated as the second volume exceeds the first, $\frac{n_2}{n_1} < 1$ implying mass is lost as the second volume is smaller than the first, and $\frac{n_2}{n_1} = 1$ implying mass-conservation.

19

S4   Semi-relaxed Sinkhorn

Calculating the gradient with respect to $\mathbf{\Pi}$

In order to run Sinkhorn, we require an initial condition on $\mathbf{\Pi}$ and an analytical expression for the gradient of our primal objective with respect to $\mathbf{\Pi}$. In particular, the following represents a primal feasible $\mathbf{\Pi}$:

$$\mathbf{\Pi}_0 = \frac{1}{n_1 n_2} \mathbf{1}_{n_1} \mathbf{1}_{n_2}^T \succcurlyeq 0,$$

$$\mathbf{\Pi}_0^T \mathbf{1}_{n_1} = \frac{1}{n_1 n_2} \mathbf{1}_{n_2} \mathbf{1}_{n_1}^T \mathbf{1}_{n_1} = \mathbf{g}_2$$

Recall that the energy function $\mathcal{E} : \mathbf{\Pi} \mapsto \mathcal{E}(\mathbf{\Pi})$ of interest in our current formulation is

$$\mathcal{E}(\mathbf{\Pi}) = \underbrace{(1-\alpha)\Big\langle \mathbf{C}, \mathbf{\Pi} \Big\rangle_F}_{\mathcal{E}_{\text{expression}}(\mathbf{\Pi})} + \underbrace{\frac{\alpha(1-\beta)}{2}\Big\langle \mathbf{L}^{\mathbf{\Psi}} \otimes \mathbf{\Pi}, \mathbf{\Pi} \Big\rangle_F}_{\mathcal{E}_{\text{GW}}^{\mathbf{\Psi}}(\mathbf{\Pi})} + \underbrace{\frac{\alpha\beta}{2}\,\text{Tr}\Big[\mathbf{\Pi}\mathbf{\Psi}^{(2)}\mathbf{\Pi}^T\Big]}_{\mathcal{E}_{\text{triplet}(1)}^{\mathbf{\Psi}^{(2)}}(\mathbf{\Pi})} + \underbrace{\frac{\alpha\beta}{2}\,\text{Tr}\Big[\mathbf{\Pi}^T\mathbf{\Psi}^{(1)}\mathbf{\Pi}\Big]}_{\mathcal{E}_{\text{triplet}(2)}^{\mathbf{\Psi}^{(1)}}(\mathbf{\Pi})} \tag{25}$$
$$+ \gamma\text{KL}(\mathbf{\Pi}\mathbf{1}_{n_2} \parallel \mathbf{g}_1) - \epsilon\text{H}(\mathbf{\Pi})$$

We calculate the gradient of f as follows. The gradient of the expression term $\mathcal{E}_{\text{expression}}(\mathbf{\Pi})$ is straightforward to compute:

$$\nabla_{\mathbf{\Pi}} \mathcal{E}_{\text{expression}}(\mathbf{\Pi}) = (1-\alpha)\mathbf{C}$$

Next, we consider the gradient of the distance-regularization term $\mathcal{E}_{\text{row}}$ corresponding to the rows of $\mathbf{\Pi}$:

$$\begin{aligned}
D\mathcal{E}_{\text{triplet}(1)}^{\mathbf{\Psi}^{(2)}}(\mathbf{\Pi}) \circ [\mathbf{V}] &= \frac{\alpha\beta}{2}\,\text{Tr}\Big[D\left(\mathbf{\Pi}\mathbf{\Psi}^{(2)}\mathbf{\Pi}^T\right) \circ [\mathbf{V}]\Big] \\
&= \frac{\alpha\beta}{2}\,\text{Tr}\Big[\mathbf{V}\mathbf{\Psi}^{(2)}\mathbf{\Pi}^T + \mathbf{\Pi}\mathbf{\Psi}^{(2)}\mathbf{V}^T\Big] \\
&= \frac{\alpha\beta}{2}\,\Big\langle \mathbf{\Pi}\left(\mathbf{\Psi}^{(2)} + (\mathbf{\Psi}^{(2)})^{\mathrm{T}}\right), \mathbf{V} \Big\rangle_F \\
&= \alpha\beta\,\Big\langle \mathbf{\Pi}\mathbf{\Psi}^{(2)}, \mathbf{V} \Big\rangle_F
\end{aligned}$$

So, we have that:

$$\nabla_{\mathbf{\Pi}} \mathcal{E}_{\text{triplet}(1)}^{\mathbf{\Psi}^{(2)}}(\mathbf{\Pi}) = \alpha\beta\mathbf{\Pi}\mathbf{\Psi}^{(2)}$$

The gradient of the distance regularization term corresponding to the columns of $\mathbf{\Pi}$ is similarly given as:

$$\nabla_{\mathbf{\Pi}} \mathcal{E}_{\text{triplet}(2)}^{\mathbf{\Psi}^{(1)}}(\mathbf{\Pi}) = \alpha\beta\mathbf{\Psi}^{(1)}\mathbf{\Pi}$$

We now compute the gradient of f_{KL}. Let $\text{proj}_{\Delta_{n_1-1}} = \left(\mathbf{I}_{n_1} - \frac{1}{n_1}\mathbf{1}_{n_1}\mathbf{1}_{n_1}^T\right)$ denote the projection onto the probability-simplex Δ_{n_1-1}

$$\begin{aligned}
Df_{\text{KL}}(\mathbf{\Pi}) \circ [\mathbf{V}] &= \gamma D\text{KL}(\mathbf{\Pi}\mathbf{1}_{n_2}\|\mathbf{g}_1) \circ [\mathbf{V}] \\
&= \gamma\left(\text{proj}_{\Delta_{n_1-1}}\left(\log\left(\mathbf{\Pi}\mathbf{1}_{n_2}\right) - \log\left(\mathbf{g}_1\right)\right)\right)^T \mathbf{V}\mathbf{1}_{n_2} \\
&= \gamma\,\text{Tr}\left(\mathbf{1}_{n_2}\left(\text{proj}_{\Delta_{n_1-1}}\left(\log\left(\mathbf{\Pi}\mathbf{1}_{n_2}\right) - \log\left(\mathbf{g}_1\right)\right)\right)^T \mathbf{V}\right)
\end{aligned}$$

With, and the $\log$ applied element-wise above. So:

$$\nabla_{\mathbf{\Pi}} f_{\text{KL}}(\mathbf{\Pi}) = \gamma\left(\mathbf{I}_{n_1} - \frac{1}{n_1}\mathbf{1}_{n_1}\mathbf{1}_{n_1}^T\right)\left(\log\left(\mathbf{\Pi}\mathbf{1}_{n_2}\right) - \log\left(\mathbf{g}_1\right)\right)\mathbf{1}_{n_2}^T$$

20

Lastly, we compute the semi-relaxed gradient for $f_{\mathrm{FGW}}(\mathbf{\Pi})$:

$$\left\langle \mathbf{L}^{\mathbf{\Psi}} \otimes \mathbf{\Pi}, \mathbf{\Pi} \right\rangle_F = \sum_{i,k,j',l'} \left(\mathbf{\Psi}^{(1)}_{ik} - \mathbf{\Psi}^{(2)}_{j'l'} \right)^2 \mathbf{\Pi}_{ij'} \mathbf{\Pi}_{kl'}$$

$$= \sum_{i,k,j',l'} \left(\mathbf{\Psi}^{(1)}_{ik} \right)^2 \mathbf{\Pi}_{ij'} \mathbf{\Pi}_{kl'} - 2 \sum_{i,k,j',l'} \mathbf{\Psi}^{(1)}_{ik} \mathbf{\Psi}^{(2)}_{j'l'} \mathbf{\Pi}_{ij'} \mathbf{\Pi}_{kl'} + \sum_{j',l'} \left(\mathbf{\Psi}^{(2)}_{j'l'} \right)^2 \left(\sum_i \mathbf{\Pi}_{ij'} \left(\sum_k \mathbf{\Pi}_{kl'} \right) \right)$$

Owing to our semi-relaxed marginalization constraints, it holds that $\sum_k \mathbf{\Pi}_{kl'} = \frac{1}{n_1}$ and $\sum_i \mathbf{\Pi}_{ij'} = \frac{1}{n_1}$, such that the rightmost term is a constant and disappears when we take the gradient with respect to $\mathbf{\Pi}$. As such, the above is proportional to:

$$\propto \sum_{i,k,j',l'} \left(\mathbf{\Psi}^{(1)}_{ik} \right)^2 \mathbf{\Pi}_{ij'} \mathbf{\Pi}_{kl'} - 2 \sum_{i,k,j',l'} \mathbf{\Psi}^{(1)}_{ik} \mathbf{\Psi}^{(2)}_{j'l'} \mathbf{\Pi}_{ij'} \mathbf{\Pi}_{kl'}$$

Converting this to matrix form, we have:

$$= \mathbf{1_{n_2}^T} \mathbf{\Pi^T} \left(\mathbf{\Psi}^{(1)} \right)^2 \mathbf{\Pi} \mathbf{1_{n_2}} - 2 \operatorname{Tr} \left[\mathbf{\Pi^T} \mathbf{\Psi}^{(1)} \mathbf{\Pi} \mathbf{\Psi}^{(2)} \right]$$

We consider each term independently. For the rightmost we consider the Fréchet derivative in the direction $\mathbf{V}$:

$$D \left(-2 \operatorname{Tr} \left[\mathbf{\Pi^T} \mathbf{\Psi}^{(1)} \mathbf{\Pi} \mathbf{\Psi}^{(2)} \right] \right) \circ [\mathbf{V}] = -2 \operatorname{Tr} \left[\mathbf{V^T} \mathbf{\Psi}^{(1)} \mathbf{\Pi} \mathbf{\Psi}^{(2)} + \mathbf{\Pi^T} \mathbf{\Psi}^{(1)} \mathbf{V} \mathbf{\Psi}^{(2)} \right] = -4 \langle \mathbf{V}, \mathbf{\Psi}^{(1)} \mathbf{\Pi} \mathbf{\Psi}^{(2)} \rangle_F$$

For the leftmost term, we have:

$$D \left(\mathbf{1_{n_2}^T} \mathbf{\Pi^T} \left(\mathbf{\Psi}^{(1)} \right)^2 \mathbf{\Pi} \mathbf{1_{n_2}} \right) \circ [\mathbf{V}] = \mathbf{1_{n_2}^T} \mathbf{\Pi^T} \left(\mathbf{\Psi}^{(1)} \right)^2 \mathbf{V} \mathbf{1_{n_2}} + \mathbf{1_{n_2}^T} \mathbf{V^T} \left(\mathbf{\Psi}^{(1)} \right)^2 \mathbf{\Pi} \mathbf{1_{n_2}}$$

$$= \operatorname{Tr} \left[\mathbf{V^T} \left(\mathbf{\Psi}^{(1)} \right)^2 \mathbf{\Pi} \mathbf{1_{n_2}} \mathbf{1_{n_2}^T} \right] + \operatorname{Tr} \left[\mathbf{1_{n_2}} \mathbf{1_{n_2}^T} \mathbf{\Pi^T} \left(\mathbf{\Psi}^{(1)} \right)^2 \mathbf{V} \right] = 2 \langle \mathbf{V}, \left(\mathbf{\Psi}^{(1)} \right)^2 \mathbf{\Pi} \mathbf{1_{n_2}} \mathbf{1_{n_2}^T} \rangle_F$$

We can therefore identify the final gradient of our semi-relaxed GW term as:

$$\nabla_{\mathbf{\Pi}} f_{\mathrm{FGW}}(\mathbf{\Pi}) = \frac{\alpha(1-\beta)}{2} \left(2 \left(\mathbf{\Psi}^{(1)} \right)^2 \mathbf{\Pi} \mathbf{1_{n_2}} \mathbf{1_{n_2}^T} - 4 \mathbf{\Psi}^{(1)} \mathbf{\Pi} \mathbf{\Psi}^{(2)} \right) = \alpha(1-\beta) \left(\left(\mathbf{\Psi}^{(1)} \right)^2 \mathbf{\Pi} \mathbf{1_{n_2}} \mathbf{1_{n_2}^T} - 2 \mathbf{\Psi}^{(1)} \mathbf{\Pi} \mathbf{\Psi}^{(2)} \right)$$

With the squaring operation applied element-wise through $\mathbf{\Psi}^{(1)}$.

S4.1 Dual formulation of semi-relaxed Sinkhorn

For our optimal-transport problem, we have both a primal objective $\mathcal{E}(\mathbf{\Pi})$ we seek to minimize, as well as a single constraint that $\mathbf{\Pi}^T \mathbf{1}_{n_1} = \mathbf{g}_2$ which restricts the set of primal-feasible $\mathbf{\Pi}$. The Karush-Kuhn-Tucker (KKT) conditions introduce a set of dual variables for each constraint, and a Lagrangian which lower bounds the primal objective. The conditions, which involve first order constraints, dual constraints, and complementary slackness constraints, offer a set of conditions which must be satisfied by an optimal solution to the primal problem. As such, we introduce the dual-variable $\boldsymbol{\mu}$, and establish the Lagrangian $\mathcal{L}$ to maximize as a lower-bound to the primal objective:

$$\mathcal{L}(\mathbf{\Pi}, \boldsymbol{\mu}) = (1-\alpha) \left\langle \mathbf{C}, \mathbf{\Pi} \right\rangle_F + \frac{\alpha}{2} \left\{ (1-\beta) \left\langle \mathbf{L}^{\mathbf{\Psi}} \otimes \mathbf{\Pi}, \mathbf{\Pi} \right\rangle_F + \beta \left(\operatorname{Tr} \left[\mathbf{\Pi} \mathbf{\Psi}^{(2)} \mathbf{\Pi}^T \right] + \operatorname{Tr} \left[\mathbf{\Pi}^T \mathbf{\Psi}^{(1)} \mathbf{\Pi} \right] \right) \right\}$$
$$+ \gamma \operatorname{KL}(\mathbf{\Pi} \mathbf{1}_n \| \mathbf{g}_1) + -\epsilon H(\mathbf{\Pi}) + \boldsymbol{\mu}^T \left(\mathbf{\Pi}^T \mathbf{1}_n - \mathbf{g}_2 \right) \quad (26)$$

Collecting the non-entropic terms in the gradient of the above expression, we define the matrix $\mathbf{C}^*$ to be:

$$\mathbf{C}^* \triangleq (1-\alpha)\mathbf{C} + \alpha \left(\mathbf{\Psi}^{(1)} \mathbf{\Pi} + \mathbf{\Pi} \mathbf{\Psi}^{(2)} \right) + \alpha(1-\beta) \left(\left(\mathbf{\Psi}^{(1)} \right)^2 \mathbf{\Pi} \mathbf{1_{n_2}} \mathbf{1_{n_2}^T} - 2 \mathbf{\Psi}^{(1)} \mathbf{\Pi} \mathbf{\Psi}^{(2)} \right)$$

The KKT conditions imply the following first-order condition holds when we consider the gradient of our Lagrangian with respect to the variable being optimized, $\mathbf{\Pi}$:

$$\nabla_{\mathbf{\Pi}} \mathcal{L}(\mathbf{\Pi}, \boldsymbol{\mu}) = \mathbf{C}^* + \gamma \left(\log(\mathbf{\Pi} \mathbf{1}_n) - \log(\mathbf{g}_1) \right) \mathbf{1}_n^T + \epsilon \log \mathbf{\Pi} + \mathbf{1}_{n'} \boldsymbol{\mu}^T = 0 \quad (27)$$

21

We also have the following primal constraint for our singular equality condition on the second marginal:

$$\mathbf{\Pi}^T \mathbf{1}_{n'} - \mathbf{g}_2 = \mathbf{0} \tag{28}$$

The dual constraints, which are implicitly accounted for in the entropy term of Sinkhorn which lifts the matrix $\mathbf{\Pi}$ through exponentiation such that $\mathbf{\Pi} \succcurlyeq \mathbf{0}$ always holds, for technical correctness include a dual variable $\mathbf{\Omega} \succcurlyeq \mathbf{0}$ and a term in the Lagrangian of the form $-\langle \Omega, \mathbf{\Pi} \rangle_F$. The two dual constraints would formally be given as:

$$\boldsymbol{\mu} \in \mathbb{R}^n \tag{29}$$

$$\mathbf{\Omega} \succcurlyeq \mathbf{0} \tag{30}$$

And a complementary slackness condition enforced elementwise through the matrix $\mathbf{\Pi}$, where one either has the active constraint where $\mathbf{\Pi}_{ij} > 0$ and $\mathbf{\Omega}_{ij} = 0$, or a slack, or inactive, constraint with $\mathbf{\Omega}_{ij} > 0$ for the (omitted) component of the Lagrangian given as $-\langle \mathbf{\Omega}, \mathbf{\Pi} \rangle_F$. Thus the slackness condition would be written as:

$$\mathbf{\Omega} \odot \mathbf{\Pi} = \mathbf{0} \tag{31}$$

Looking more closely at the first-order conditions, one finds:

$$(\mathbf{C}^*)_{i,j} + \gamma \left(\log\left(\mathbf{\Pi}_{i,.}^T \mathbf{1}_n\right) - \log(\mathbf{g}_{1,i}) \right) + \epsilon \log \mathbf{\Pi}_{i,j} + \boldsymbol{\mu}_j = \mathbf{0}$$

Implying a similar solution-form to Sinkhorn involving an exponentiation with the Gibbs kernel, wherein one has $\mathbf{K}_{i,j} = e^{-\epsilon^{-1}\mathbf{C}_{i,j}^*}$ and:

$$\mathbf{\Pi}_{i,j} = e^{-\frac{\gamma}{\gamma+\epsilon} \log\left(\frac{\mathbf{\Pi}_{i,.}^T \mathbf{1}_n}{\mathbf{g}_{1,i}}\right)^{(\gamma+\epsilon)/\epsilon}} \mathbf{K}_{i,j} e^{-\epsilon^{-1}\boldsymbol{\mu}_j}$$

From Sinkhorn, we know there exist unique vectors $\mathbf{u}, \mathbf{v}$ such that $\mathbf{\Pi} = \operatorname{diag}(\mathbf{u}) \mathbf{K} \operatorname{diag}(\mathbf{v})$ and see:

$$\mathbf{\Pi} = \operatorname{diag}\left(e^{\frac{-\gamma}{\epsilon} \log(\mathbf{\Pi}\mathbf{1_n}/\mathbf{g_1})}\right) \mathbf{K} \operatorname{diag}\left(e^{-\epsilon^{-1}\boldsymbol{\mu}}\right) \triangleq \operatorname{diag}(\mathbf{u}) \mathbf{K} \operatorname{diag}(\mathbf{v})$$

We consider what the update rule should be, given this identification, by establishing:

$$\mathbf{u} = e^{\frac{-\gamma}{\epsilon} \log(\mathbf{\Pi}\mathbf{1_n}/\mathbf{g_1})} = \left(\frac{\mathbf{\Pi}\mathbf{1_n}}{\mathbf{g_1}}\right)^{-\gamma/\epsilon} = \left(\frac{\operatorname{diag}(\mathbf{u}) \mathbf{K} \operatorname{diag}(\mathbf{v})\mathbf{1_n}}{\mathbf{g_1}}\right)^{-\gamma/\epsilon}$$

$$= \left(\frac{\mathbf{u} \odot \mathbf{Kv}}{\mathbf{g_1}}\right)^{-\gamma/\epsilon} = \mathbf{u}^{-\gamma/\epsilon} \odot \left(\frac{\mathbf{Kv}}{\mathbf{g_1}}\right)^{-\gamma/\epsilon}$$

Noting the Hadamard multiplication, this directly implies an update rule for $\mathbf{u}$ in the form:

$$\mathbf{u} = \left(\left(\frac{\mathbf{Kv}}{\mathbf{g_1}}\right)^{-\gamma/\epsilon}\right)^{\frac{\epsilon}{\gamma+\epsilon}} = \left(\frac{\mathbf{g_1}}{\mathbf{Kv}}\right)^{\frac{\gamma}{\gamma+\epsilon}}$$

This may analogously be identified from the general form of unbalanced optimal transport, wherein one uses an anisotropic proximal step weighting two divergences on the marginals $\mathbf{g_1}$. In particular, for a generalized optimal transport problem of the form:

$$\inf_{\mathbf{\Pi}} \langle \mathbf{C}, \mathbf{\Pi} \rangle_F + \lambda_1 \mathrm{D}_{\varphi_1}(\mathbf{\Pi}\mathbf{1}_{n_2}|\mathbf{g_1}) + \lambda_2 \mathrm{D}_{\varphi_2}(\mathbf{\Pi}^T \mathbf{1}_{n_1}|\mathbf{g_2}) + \epsilon H(\mathbf{\Pi})$$

for φ_1, φ_2 convex, positive lower-semi-continuous divergences. For these, one takes a proximal step for each marginal where $\mathbf{u}, \mathbf{v}$ are updated as:

$$\mathbf{u} = \operatorname{argmin}_{\mathbf{u}'} \mathrm{KL}(\mathbf{u}'||\mathbf{u}) + \frac{\lambda_1}{\epsilon}\mathrm{D}_{\varphi_1}(\mathbf{u}'||\mathbf{g_1})$$

$$\mathbf{v} = \operatorname{argmin}_{\mathbf{v}'} \mathrm{KL}(\mathbf{v}'||\mathbf{v}) + \frac{\lambda_2}{\epsilon}\mathrm{D}_{\varphi_2}(\mathbf{v}'||\mathbf{g_2})$$

22

This has the following closed-form updates for unbalanced Sinkhorn where we consider the case that $D_{\varphi_1}, D_{\varphi_2}$ are taken to be KL-divergences:

$$\mathbf{u}^{(l+1)} = \left(\frac{\mathbf{g}_1}{\mathbf{K}\mathbf{v}^{(l)}}\right)^{\frac{\lambda_1}{\lambda_1+\epsilon}}$$

$$\mathbf{v}^{(l+1)} = \left(\frac{\mathbf{g}_2}{\mathbf{K}^T\mathbf{u}^{(l+1)}}\right)^{\frac{\lambda_2}{\lambda_2+\epsilon}}$$

While we demonstrated that the semi-relaxed update follows directly from the KKT conditions, one can easily recover the semi-relaxed update in the limit of $\lambda_2 \to \infty$ in the unbalanced case. The marginal update then becomes $\mathbf{v}^{(l+1)} = \lim_{\lambda_2\to\infty}\left(\frac{\mathbf{g}_2}{\mathbf{K}^T\mathbf{u}^{(l+1)}}\right)^{\frac{\lambda_2}{\lambda_2+\epsilon}} = \frac{\mathbf{g}_2}{\mathbf{K}^T\mathbf{u}^{(l+1)}}$, where one recovers the marginal constraint on $\mathbf{g}_2$ and our semi-relaxed update rule.

S4.2 Converting semi-relaxed Sinkhorn to log-domain for stability

Consider a general form of entropy-regularized, fully unbalanced Wasserstein optimal transport: given measures $\mathbf{g}_1 \in \mathbb{R}^{n_1}_+, \mathbf{g}_2 \in \mathbb{R}^{n_2}_+$, and given a candidate transport plan $\mathbf{\Pi} \in \mathbb{R}^{n_1 \times n_2}_+$, let the functional $\mathbf{\Pi} \mapsto \mathcal{P}_\epsilon(\mathbf{\Pi})$ be given by

$$\mathcal{P}_\epsilon(\mathbf{\Pi}) = \langle \mathbf{C}, \mathbf{\Pi} \rangle_F + D_{\varphi_1}(\mathbf{\Pi}\mathbf{1}_{n_2}|\mathbf{g}_1) + D_{\varphi_1}(\mathbf{\Pi}^T\mathbf{1}_{n_1}|\mathbf{g}_2) + \epsilon H(\mathbf{\Pi}) \tag{32}$$

where φ_1, φ_2 are convex, positive lower-semi-continuous, and with $\varphi_i(1) = 0$. The terms D_{φ_i} are the associated φ-divergences. Depending on the choice of the φ_i, one can recover either the fully unbalanced constraints of moscot, or the semi-relaxed setting of DeST-OT. Specifically, moscot corresponds to taking $\varphi_1 = \varphi_2 \equiv p \mapsto p\log p - p + 1$, in which case both φ-divergences are the KL divergence. On the other hand, DeST-OT corresponds to taking $\varphi_1 \equiv p \mapsto p\log p - p + 1$, while the single hard constraint corresponds to choosing $\varphi_2 = \iota_{\{1\}}$, where

$$\iota_{\{1\}}(p) = \begin{cases} 0 & p = 1 \\ +\infty & \text{otherwise.} \end{cases}$$

Thus, (32) corresponds to a version of the moscot objective (3) with the GW term $\langle \mathbf{L} \otimes \mathbf{\Pi}, \mathbf{\Pi} \rangle$ omitted, or a version of the DeST-OT objective (22) without our modified GW term $\langle \widetilde{\mathbf{L}}^{\mathbf{M}} \otimes \mathbf{\Pi}, \mathbf{\Pi} \rangle$. In both cases, the hyperparameters attached to different terms have been suppressed.

We define $OT_\epsilon(\mathbf{g}_1, \mathbf{g}_2) = \inf_{\mathbf{\Pi}\in\mathbb{R}^{n_1\times n_2}_+} \mathcal{P}_\epsilon(\mathbf{\Pi})$, and we appeal to the dual formulation of (32), which we state as a proposition.

Proposition 1 ([36], Proposition 2). *One has*

$$OT_\epsilon(\mathbf{g}_1, \mathbf{g}_2) = \sup_{\mathbf{f}\in\mathbb{R}^{n_1}_+, \mathbf{g}\in\mathbb{R}^{n_2}_+} \mathcal{D}_\epsilon(\mathbf{f}, \mathbf{g}),$$

where for such $\mathbf{f} \in \mathbb{R}^{n_1}_+, \mathbf{g} \in \mathbb{R}^{n_2}_+$, we define the dual objective to $\mathcal{P}_\epsilon$ (32)

$$\mathcal{D}_\epsilon(\mathbf{f}, \boldsymbol{\mu}) = -\langle \varphi_1^*(-\mathbf{f}), \mathbf{g}_1 \rangle_F - \langle \varphi_2^*(-\boldsymbol{\mu}), \mathbf{g}_2 \rangle_F - \epsilon e^{\mathbf{f}/\epsilon} \odot e^{-\mathbf{C}/\epsilon} \odot e^{\boldsymbol{\mu}/\epsilon},$$

where $(\varphi_1^*, \varphi_2^*)$ are the Legendre transforms of (φ_1, φ_2), namely $\varphi_i^*(q) = \sup_{p\geq 0} pq - \varphi_i(p)$

The optimal primal plan $\mathbf{\Pi}^\star$ is obtained from the optimal pair $(\mathbf{f}^\star, \boldsymbol{\mu}^\star)$ of dual variables as

$$\mathbf{\Pi}^\star = \text{diag}(e^{\mathbf{f}^\star/\epsilon})e^{-\mathbf{C}/\epsilon}\text{diag}(e^{\boldsymbol{\mu}^\star/\epsilon}) = \text{diag}(\mathbf{u})e^{-\mathbf{C}/\epsilon}\text{diag}(\mathbf{v})$$

Thus, connecting the dual variables of the generalized Sinkhorn objective for arbitrary φ-divergences to our primal variables $\mathbf{u}, \mathbf{v}$, we are able to express closed-form updates for the dual variables instead. The Sinkhorn iterations for the semi-relaxed case, in terms of the dual variables $\mathbf{f}, \mathbf{g}$ are given as:

$$\mathbf{f}^{(l+1)} = \epsilon\log\mathbf{u}^{(l)} = \epsilon\log\left(\frac{\mathbf{g}_1}{\mathbf{K}\mathbf{v}}\right)^{\frac{\gamma}{\gamma+\epsilon}} = \frac{\gamma}{\gamma+\epsilon}\left(\epsilon\log\mathbf{g}_1 - \epsilon\log\left(\mathbf{K}e^{\boldsymbol{\mu}^{(l)}/\epsilon}\right)\right) \tag{33}$$

23

$$\boldsymbol{\mu}^{(l+1)} = \epsilon \log \mathbf{g}_2 - \epsilon \log \left(\mathbf{K}^T e^{\mathbf{f}^{(l+1)}/\epsilon} \right) \tag{34}$$

Owing to the presence of the exponential of each dual variable on the right-hand side of 33 and 34, these cannot be evaluated directly for small values of the entropy-regularization ϵ. When $\epsilon \to 0$ we would recover an exact, non entropically-regularized optimal transport – however, this would cause the term inside of the logarithm to exceed numerical precision. For the purpose of introducing the log-domain Sinkhorn algorithm, we make the following definitions. For $\mathbf{1}_{n_i} \in \mathbb{R}_+^{n_i}$ and $\epsilon > 0$, the *Softmin operators* $\mathrm{Smin}_\epsilon^{\mathbf{g}_i}$ are defined for any vectors $\mathbf{f} \in \mathbb{R}^{n_1}$ and $\boldsymbol{\mu} \in \mathbb{R}^{n_2}$ by:

$$\mathrm{Smin}_\epsilon^{\mathbf{1}_{n_1}}(\mathbf{f}) = -\epsilon \log \left(\left\langle e^{-\mathbf{f}/\epsilon}, \mathbf{1}_{n_1} \right\rangle \right) \quad \text{and} \quad \mathrm{Smin}_\epsilon^{\mathbf{1}_{n_2}}(\boldsymbol{\mu}) = -\epsilon \log \left(\left\langle e^{-\boldsymbol{\mu}/\epsilon}, \mathbf{1}_{n_2} \right\rangle \right)$$

Rewriting 34 34 we see:

$$\mathbf{f}_i^{(l+1)} = \frac{\gamma}{\gamma + \epsilon} \left(\epsilon \log \mathbf{g}_{1i} - \epsilon \log \left(\langle e^{-\mathbf{C}_{i,.}/\epsilon}, e^{\boldsymbol{\mu}^{(l)}/\epsilon} \rangle \right) \right) = \frac{\gamma}{\gamma + \epsilon} \left(\epsilon \log \mathbf{g}_{1i} + \mathrm{Smin}_\epsilon^{\mathbf{1}_{n_1}} \left(\mathbf{C}_{ij} - \boldsymbol{\mu}_j \right)_j \right)$$

And:

$$\boldsymbol{\mu}_j^{(l+1)} = \epsilon \log \mathbf{g}_2 - \epsilon \log \left(\langle e^{-\mathbf{C}_{.,j}/\epsilon}, e^{\mathbf{f}^{(l+1)}/\epsilon} \rangle \right) = \epsilon \log \mathbf{g}_{2j} + \mathrm{Smin}_\epsilon^{\mathbf{1}_{n_1}} \left(\mathbf{C}_{ij} - \mathbf{f}_i \right)_i$$

One can simply evaluate the softmin $\mathrm{Smin}_\epsilon^{\mathbf{1}_{n_1}}$ using the log-sum-exp trick, which we broadcast across dimensions for an efficient and stable log-domain update.

S5   Metrics of growth

Let $\mathcal{S}_1 = (\mathbf{S}_1, \mathbf{X}_1)$ and $\mathcal{S}_2 = (\mathbf{S}_2, \mathbf{X}_2)$ be a pair of spatiotemporal tissue slices, corresponding to timepoints t_1 and t_2. For a collection of cell types shared across both slices, enumerated as $\{1, \ldots, P\}$, suppose we are given cell type partitions $\mathcal{P}_1 = \{\mathcal{P}_1(p)\}_{p=1}^P$ and $\mathcal{P}_2 = \{\mathcal{P}_2(p)\}_{p=1}^P$ for each slice. The *mass of cell type p at time t_1* is $m_1(p) = |\mathcal{P}_1(p)|$, and the *mass of cell type p at time t_2* is likewise $m_2(p) = |\mathcal{P}_t(p)|$. The *mass-flux of cell type p* over these two timepoints is then given by $m_2(p) - m_1(p)$. Below, we define a metric quantifying how well the cell type mass-flux inferred by an optimal transport method matches the empirical mass-flux of a cell type. If such a method outputs a pair $(\boldsymbol{\Pi}, \boldsymbol{\xi})$ of an alignment matrix and a growth vector, we measure the distortion between $\boldsymbol{\xi}$ and the true mass flux. We discuss the assumptions that go into this metric, and how it can be generalized.

S5.1   A metric of growth: individual cell level

To measure the accuracy of the growth rates across cell types *and* spots within the cell type, we define the true growth rate at time t_1 of cell type p as:

$$\gamma_1(p) = \frac{1}{m_1(p)} \left(\frac{m_2(p) - m_1(p)}{n_1} \right) \tag{35}$$

In calling this a true growth rate, we are making two assumptions: first, that there are no cell type transitions between distinct cell types – in the next subsection we discuss how to relax this. The second assumption made is that the burden of accomplishing the change in mass is shared equally across cells of the same type, which can be viewed as an entropy-maximizing assumption.

The normalization factor $\frac{1}{n_1}$ makes these growth-rates consistent with the slice one mass-normalized values of the marginals $\mathbf{g}_1, \mathbf{g}_2$ and ensures consistency across experiments. We quantify the total distortion between the true growth factors for each cell type and those derived from optimal transport as:

$$\mathcal{J}_{growth} = \sum_{p=1}^P \sum_{i \in \mathcal{P}_1(p)} \|\boldsymbol{\xi}_i - \gamma_1(p)\|_2^2 \tag{36}$$

This assesses the total divergence between the optimal-transport growth rates and the true, empirical growth rates under a fixed cell type labeling. The sum of the growth-rates across spots within a tissue slice equals the total growth rate of

24

the slice:

$$\sum_{p=1}^{P} \sum_{i \in \mathcal{P}_1(p)} \gamma_1(p) = \frac{1}{n_1} \sum_{p=1}^{P} \sum_{i \in \mathcal{P}_1^{(p)}} \left(\frac{m_2(p) - m_1(p)}{m_1(p)} \right)$$

$$= \frac{1}{n_1} \sum_{p=1}^{P} \left(m_2(p) - m_1(p) \right)$$

$$= \frac{n_2 - n_1}{n_1}.$$

S5.2 Generalizing the growth-metric to cell type transitions

The definition of growth given in the section above assumes that cells of type p transition and grow to their own cell type, and computes the distortion relative to this assumption. While this is valuable as a baseline metric when no cell type transitions are available, we generalize this notion when we have a density matrix of cell-to-cell reverse-time transitions $\mathbf{T} \in \mathbb{R}_{\geq 0}^{P \times P}$ across P cell types. Supposing we have a vector $\mathbf{m}_2 \in \mathbb{R}_{\geq 0}^{P}$ of cell type masses at time t_2, and likewise $\mathbf{m}_1$ at time t_1, we modify $m_1(p)$ in the definition above to include transitions. The section above implicitly assumes that the matrix is diagonal (in particular, it is the $P \times P$ identity matrix $\mathbf{T} = \mathbb{1}_P$). Under ground truth transition matrix $\mathbf{T}$, the mass of cell type p from time at time t_1 is described in terms of $\mathbf{m}_2$ as follows:

$$m_1(p) = \langle \mathbf{T}_{p,\cdot}, \mathbf{m}_2 \rangle \tag{37}$$

Which is to say, $\mathbf{m}_1$ can be described in terms of $\mathbf{m}_2$ via the matrix-multiplication

$$\mathbf{m}_1 = \mathbf{T}\mathbf{m}_2 \tag{38}$$

and the mass-flux out of cell type p remains as defined in the previous sections with the only adjustment being that the new $m_1(p)$'s account for cell type transitions. As before, we assume the cell type partitions across each slice are consistent with these cell type mass vectors.

Now, consider an alignment matrix $\mathbf{\Pi} \in \mathbb{R}^{n_1 \times n_2}$, and let $\{p \to q\}$ denote the following set:

$$\{p \to q\} = \bigcup_{\substack{i \in \mathcal{P}_1(p) \\ j' \in \mathcal{P}_2(q)}} \{(i, j')\},$$

understood as the event that cell type p of the first slice is mapped to cell type q in the second slice. In making this definition, we show how any alignment matrix $\mathbf{\Pi}$ induces a reverse-time transition matrix: indeed, $\mathbf{\Pi}$ is a positive measure on such pairs, so one can naturally form a coarse-grained $P \times P$ matrix from $\mathbf{\Pi}$ using the events $\{p \to q\}$: first, define

$$\mathbb{R}_{\geq 0}^{P \times P} \ni \overline{\mathbf{\Pi}}, \quad \overline{\mathbf{\Pi}}_{pq} := \mathbf{\Pi}(p \to q)$$

Whatever $\mathbf{T}$ we construct from $\mathbf{\Pi}$ should be a transition matrix, row-normalized such that $\mathbb{1}_P = \mathbf{T}\mathbb{1}_P$. This is achieved by tilting each row p of measure $\overline{\mathbf{\Pi}}$ with the factor $n_1/m_2(q)$:

$$\mathbf{T}_{pq}^{\star} = \left(\frac{n_1}{m_2(q)} \right) \overline{\mathbf{\Pi}}_{pq}. \tag{39}$$

Now, consider the distortion metric defined in (36). Instead of viewing $\mathcal{J}_{growth}$ as a function of $\boldsymbol{\xi}$ only, as was done in the previous section, we now regard it as a function of both $\boldsymbol{\xi}$ and $\gamma_1 \equiv (\gamma_1(p))_{p=1}^{P}$. Just as $\boldsymbol{\xi}$ arises from $\mathbf{\Pi}$, vector γ_1 is defined from $\mathbf{T}$ through (37) and (35). Given the output $(\mathbf{\Pi}, \boldsymbol{\xi})$ of an OT method, the next proposition gives the optimal pair $(\mathbf{T}, \gamma_1)$ for this output according to the growth distortion metric (36).

Proposition 2. *Given cell type partitions $\mathcal{P}_1$ and $\mathcal{P}_2$ of two SRT slices, let $\mathbf{m}_1$ and $\mathbf{m}_2$ be a pair of cell type mass vectors consistent with these partitions, and related by a transition matrix $\mathbf{T}$ through (38). Fix an alignment matrix $\mathbf{\Pi}$ with $\mathbf{\Pi}^T \mathbf{1}_{n_1} = \frac{1}{n_1} \mathbf{1}_{n_2}$ and consider its associated growth vector $\boldsymbol{\xi} \equiv \boldsymbol{\xi}(\mathbf{\Pi})$. Then, for $\gamma_1 \equiv \gamma_1(\mathbf{T})$, one has*

$$\mathbf{T}^{\star} = \mathrm{argmin}_{(\mathbf{T}, \gamma_1(\mathbf{T}))} \mathcal{J}_{growth}(\boldsymbol{\xi}, \gamma_1),$$

with $\mathbf{T}^{\star}$ defined from $\mathbf{\Pi}$ in (39).

25

Proof. When $\boldsymbol{\xi}$ is fixed, the minimizer of 36, in terms of $\boldsymbol{\gamma}_1$, is given in each entry by the cell type sample mean of $\boldsymbol{\xi}$:

$$\gamma_1^\star(p) = \frac{1}{m_1(p)} \sum_{i \in \mathcal{P}_1(p)} \xi_i$$

Thus, we evaluate the right-hand side to find:

$$\frac{1}{m_1(p)} \sum_{i \in \mathcal{P}_1(p)} \xi_i = \frac{1}{m_1(p)} \sum_{i \in \mathcal{P}_1(p)} \left(\boldsymbol{\Pi}_{i,\cdot}^T \mathbf{1}_{n_1} - \frac{1}{n_1} \right) \tag{40}$$

$$= \frac{1}{m_1(p)} \sum_{i \in \mathcal{P}_1(p)} \boldsymbol{\Pi}_{i,\cdot}^T \mathbf{1}_{n_1} - \frac{1}{n_1} \tag{41}$$

$$= \frac{1}{n_1} \frac{m_2(p)}{m_1(p)} - \frac{1}{n_1} \tag{42}$$

Therefore, we have that:

$$\frac{1}{m_1(p)} \sum_{i \in \mathcal{P}_1(p)} \boldsymbol{\Pi}_{i,\cdot}^T \mathbf{1}_{n_1} = \frac{1}{n_1} \frac{m_2(p)}{m_1(p)}$$

And we decompose the following sum according to the cell types p may transition to in the next slice:

$$n_1 \sum_{i \in \mathcal{P}_1(p)} \boldsymbol{\Pi}_{i,\cdot}^T \mathbf{1}_{n_1} = \sum_{q=1}^{P} n_1 \overline{\boldsymbol{\Pi}}_{pq} \tag{43}$$

$$= \sum_{q=1}^{P} m_2(q) \cdot \frac{n_1}{m_2(q)} \overline{\boldsymbol{\Pi}}_{pq} \tag{44}$$

$$\equiv \mathbf{T}_{p,\cdot}^\star \mathbf{m}_2, \tag{45}$$

which shows that the optimal $\boldsymbol{\gamma}_1^\star$ arises from the claimed optimal transition matrix $\mathbf{T}^\star$ defined in (39) We complete the proof by checking that each row of $\mathbf{T}$ sums to one. For notational convenience let $\mathbf{z}_2(q)$ denote the vector in $\mathbb{R}^{n_2}$ whose j'-th component has a 1 if and only if $j' \in \mathcal{P}_2(q)$, and is 0 otherwise; likewise, let $\mathbf{z}_1(p)$ be the vector in $\mathbb{R}^{n_1}$ which is a one-hot encoding of cell type p over the first slice.

$$\sum_{p=1}^{P} \mathbf{T}_{pq} = \frac{n_1}{m_2(q)} \sum_{p=1}^{P} \overline{\boldsymbol{\Pi}}(p \to q) \tag{46}$$

$$= \frac{n_1}{m_2(q)} \sum_{p=1}^{P} \mathbf{z}_1(p)^T \boldsymbol{\Pi} \mathbf{z}_2(q) \tag{47}$$

$$= \frac{n_1}{m_2(q)} \mathbf{1}_{n_1}^T \boldsymbol{\Pi} \mathbf{z}_2(q) \tag{48}$$

The last step is to use the single hard constraint in our semi-relaxed formulation, along with our choice of mass calibration for the second slice: $\boldsymbol{\Pi}^T \mathbf{1}_{n_1} = \frac{1}{n_1} \mathbf{1}_{n_2}$. Continuing from the above display, one has

$$\frac{n_1}{m_2(q)} \left(\boldsymbol{\Pi}^T \mathbf{1}_{n_1} \right)^T \mathbf{z}_2(q) = \frac{n_1}{m_2(q)} \frac{1}{n_1} \mathbf{1}_{n_2}^T \mathbf{z}_2(q) = 1.$$

By definition, all entries of $\mathbf{T}$ are necessarily positive. Therefore these row-sum conditions show us this is indeed a reverse-time transition matrix, and the proof is finished. $\square$

S5.3 Interpretation of per-cell growth distortion $\mathcal{J}_{growth}$

For the setting of $\gamma_1(p)$ in the previous section, rather than matching the cell type mass-fluxes assuming cell types transitioning to themselves, we find the optimal matrix $\mathbf{T}$ of cell types transitioning from t_1 to t_2, calculate the adjusted

mass contributed to $\mathbf{m}_2$ from cell type p at t_1 as $m_1(p) = \mathbf{T}_{p,.}\mathbf{m}_2$, and calculate the expected distortion in the mass-flux. As noted in 2, the minimizer of $\mathcal{J}_{growth}$ over $\boldsymbol{\gamma}_1$ is simply the sample mean of the per-cell type mass-flux, given as:

$$\gamma_1(p) = \frac{1}{m_1(p)} \sum_{i \in \mathcal{P}_1(p)} \xi_i.$$

Therefore an alternative interpretation to one in which we match the mass-flux of the optimal transition matrix is that we are measuring the sum of the variances of each mass-flux variable within each cell type:

$$\sum_{\substack{\text{(cell types) } p=1}}^{P} \mathbf{Var}\left(\boldsymbol{\xi}_i \mid i \in \mathcal{P}_1(p)\right)$$

In a tissue or cell type, the assumption that growth is relatively homogeneous or smoothly varying, as opposed to coming from a very small, sparse, set of cells, has been observed in morphogen studies where within tissues like the imaginal wing disk in drosophila one observes uniform cell divisions and growth [15] [25] [27]. As such, measuring the within-cell type variance of the growth-factors is biologically reasonable and captures whether growth patterns are very sparse (i.e. when aligned via an unbalanced routine which assigns a few "representative" cells as those which grow), or whether growth patterns are relatively consistent.

S6 Procrustes-like problems and a cell migration metric

S6.1 Quantifying a metric of naive rigid-body migration

Suppose we are given the solution to either the generalized Procrustes' problem for an orthogonal transformation $\mathbf{Q} \in \mathrm{O}(n)$ or the generalized Wahba's problem for a rotation $\mathbf{Q} \in \mathrm{SO}(n)$ along with a general translation vector $\mathbf{h} \in \mathbb{R}^n$ as described in S6.3. This then describes a simple rigid-body transformation which relates the coordinate frames of slice 1 and 2, $\mathcal{S}_1 \approx \tilde{\mathcal{S}}_2 = \{\mathbf{Q}\left(\mathbf{s}'_{j'} - \mathbf{h}\right) : \mathbf{s}'_{j'} \in \mathcal{S}_2\}$. Supposing the true transformation relating the two frames is indeed a rigid-body transformation, one may directly quantify the cost of an alignment with respect to the matrix $\mathbf{\Pi}$ given $\mathbf{Q}, \mathbf{h}$. We introduce this as our *naive rigid-body migration* metric, given as:

$$\sum_{i=1}^{n_1} \left(\mathbf{\Pi}_{i,.}^T \mathbf{1}_{n_2}\right)^{-1} \left(\sum_{j'=1}^{n_2} \mathbf{\Pi}_{ij'} \|\mathbf{s}_i - \mathbf{Q}\left(\mathbf{s}'_{j'} - \mathbf{h}\right)\|_2^2\right) \tag{49}$$

Where we take the difference between the spatial points $\mathbf{s}_i$ and $\mathbf{s}'_{j'}$ in our pair of slices $(\mathbf{X}^{(1)}, \mathbf{S}^{(1)})$ and $(\mathbf{X}^{(2)}, \mathbf{S}^{(2)})$. This difference is computed under the posterior implied by $\mathbf{\Pi}$, and as we compare matrices $\mathbf{\Pi}$ which may be balanced, unbalanced, or semi-relaxed, we normalize by a factor of $\mathbf{\Pi}_{i,.}^T \mathbf{1}_{n_2}$ so that any posterior in 49 is normalized to a distribution consistently. We call this metric *naive*, as it is clear this transformation has determinant 1, and neither allows for volume expansion (growth) or volume shrinkage (death). Moreover, the true transformation underlying tissue development might involve some arbitrary (e.g. diffeomorphic) transformation, such that the rigid-body assumption is more generally inappropriate. As such, it is not necessarily the case that lower loss under this metric is universally better. However, one can say that if the alignment tends to incur exceptionally high loss under this metric, without any geometric consistency, the alignment may be spatially unrealistic. In other words, it might be aligning the sub-level set of points with similar features $\Omega_{\mathbf{x}'_{j'}} = \{\mathbf{s}_i \in \mathcal{S}_1 : \|\mathbf{s}_i - \mathbf{s}'_{j'}\|_2^2 \leq (\text{const.})\}$ without accounting for the geometry of either slice.

S6.2 Invariance of the method to rigid-body transformations, or group action by members of SE(2)

Let us call each spatial point in the first slice $\mathbf{s}_i \in \mathbb{R}^2$, and each point in the second slice $\mathbf{s}'_{j'} \in \mathbb{R}^2$. Suppose we want the second slice to be in the same coordinate basis as the first slice, but we do not know $\mathbf{Q} \in \mathrm{SE}(2), \mathbf{h} \in \mathbb{R}^2$, representing the rigid-body transformation of the data $\tilde{\mathbf{s}}_{j'} = \mathbf{Q}(\mathbf{s}'_{j'} - h)$ which moves us into the correct, shared coordinate-frame. A reasonable question to ask is whether our objective returns an alignment matrix $\mathbf{\Pi}$ which is unique, independent of the specific $\mathbf{Q}, \mathbf{h}$ that relate the two coordinate frames. From the general objective in 20, it is clear that our objective only depends on the points in the first and second slices $\mathbf{s}_i, \mathbf{s}'_{j'}$ through the distance matrices $\mathbf{D}^{(1)}$ and $\mathbf{D}^{(2)}$. Considering that $\mathbf{s}_i$ is in the correct basis, let us restrict our attention to $\mathbf{s}'_{j'}$ and $\mathbf{D}^{(2)}$. It is simple to check that:

$$[\mathbf{D}^{(2)}]_{i'j'} = \|\mathbf{s}'_{i'} - \mathbf{s}'_{j'}\|_2 = \|\mathbf{Q}\mathbf{s}'_{i'} - \mathbf{Q}\mathbf{s}'_{j'}\|_2 = \|\tilde{\mathbf{s}}_{i'} - \tilde{\mathbf{s}}_{j'}\|_2$$

Which implies that our objective does not depend on the spatial location or rotation of the second slice relative to the first. Uniqueness therefore only depends on the convexity of the objective, which could in principle be achieved by using the projection of $\mathbf{D}^{(1)}$, $\mathbf{D}^{(2)}$ onto the vector space of positive-semi definite matrices $\mathcal{S}_n^+$ or kernelization.

The next reasonable question is whether one can recover the correct $\mathbf{Q}$, $\mathbf{h}$ given the alignment matrix $\mathbf{\Pi}$. Problems of this form include the Orthogonal Procrustes problem (where $\mathbf{Q}$ is simply an orthogonal matrix), and Wahba's problem (where $\mathbf{Q} \in \mathrm{SO}(2)$ explicitly), which are both well studied and have existing solution methods. Thus, the final problem needed to align the coordinate frame can be given (in Procrustes' form) as:

$$\min_{\mathbf{Q}\in\mathbb{R}^{2\times 2},\,\mathbf{h}\in\mathbb{R}^2} \quad \sum_{i,j'}\mathbf{\Pi}_{ij'}\|\mathbf{s}_i - \mathbf{Q}(\mathbf{s}'_{j'} - \mathbf{h})\|_2^2$$
$$\text{s.t.} \quad \mathbf{Q}^{\mathbf{T}}\mathbf{Q} = \mathbb{1}_2 \tag{50}$$

Or, in Wahba's problem form:

$$\min_{\mathbf{Q}\in\mathrm{SO}(2),\,\mathbf{h}\in\mathbb{R}^2} \quad \sum_{i,j'}\mathbf{\Pi}_{ij'}\|\mathbf{s}_i - \mathbf{Q}(\mathbf{s}'_{j'} - \mathbf{h})\|_2^2 \tag{51}$$

We offer both the Procrustes' and Wahba's form, with the latter having the restriction that $\mathbf{Q} \in \mathrm{SO}(2)$ requires $\det \mathbf{Q} = 1$, which is to say we seek an explicit (orientation-preserving) rotation rather than a general orthogonal transformation (which may be a rotation composed with a reflection). In either case, the problem of finding a correct alignment is something that emerges *after* the outputs of DeST-OT, which is itself completely independent of the coordinate frame the first and second slice are set in and is invariant to linear translation and rotation, unlike works involving Gaussian processes such as [18].

S6.3 Review of the Solution to Wahba's problem

First, we consider an appropriate transformation of the coordinates to eliminate the dependence on the translation, for this light generalization of Wahba's problem to a joint-distribution across both slices [10]. In particular, consider the change of variables given by:

$$\mathbf{h} = -\mathbf{Q}^T\mathbf{s}_{\mathrm{cm}} + \mathbf{s}'_{\mathrm{cm}} + \boldsymbol{\nu}$$

For $\mathbf{s}_{\mathrm{cm}}, \mathbf{s}'_{\mathrm{cm}}$ representing the center of mass of slice 1 and slice 2, and $\boldsymbol{\nu}$ an undetermined constant. In particular,

$$\mathbf{s}_{\mathrm{cm}} = \left(\mathbf{1}_{n_1}^T\mathbf{\Pi}\mathbf{1}_{n_2}\right)^{-1}\sum_{i=1}^{n_1}\sum_{j'=1}^{n_2}\mathbf{\Pi}_{ij'}\mathbf{s}_i, \qquad \mathbf{s}'_{\mathrm{cm}} = \left(\mathbf{1}_{n_1}^T\mathbf{\Pi}\mathbf{1}_{n_2}\right)^{-1}\sum_{i=1}^{n_1}\sum_{j'=1}^{n_2}\mathbf{\Pi}_{ij'}\mathbf{s}'_{j'} \tag{52}$$

Substituting this into the primal objective:

$$\sum_{i,j'}\mathbf{\Pi}_{ij'}\|\mathbf{s}_i - \mathbf{Q}(\mathbf{s}'_{j'} - \mathbf{h})\|_2^2 = \sum_{i,j'}\mathbf{\Pi}_{ij'}\|\mathbf{s}_i - \mathbf{Q}(\mathbf{x}'_{j'} - (-\mathbf{Q}^T\mathbf{s}_{\mathrm{cm}} + \mathbf{s}'_{\mathrm{cm}} + \boldsymbol{\nu}))\|_2^2$$

$$= \|\boldsymbol{\nu}\|_2^2(\mathbf{1}_{n_1}^T\mathbf{\Pi}\mathbf{1}_{n_2}) + \sum_{i,j'}\mathbf{\Pi}_{ij'}\|(\mathbf{s}_i - \mathbf{s}_{\mathrm{cm}}) - \mathbf{Q}(\mathbf{s}'_{j'} - \mathbf{s}'_{cm})\|_2^2$$

$$+ \boldsymbol{\nu}^T\left(\left(\sum_{i,j'}\mathbf{\Pi}_{ij'}\mathbf{s}_i - (\mathbf{1}_{n_1}^T\mathbf{\Pi}\mathbf{1}_{n_2})\mathbf{s}_{\mathrm{cm}}\right) + \left(\sum_{i,j'}\mathbf{\Pi}_{ij'}\mathbf{s}'_{j'} - (\mathbf{1}_{n_1}^T\mathbf{\Pi}\mathbf{1}_{n_2})\mathbf{s}'_{\mathrm{cm}}\right)\right)$$

By definition of the center of mass-coordinates, the above equates to the following, with the minimization over $\mathbf{r}$ now over $\boldsymbol{\nu}$:

$$\min_{\mathbf{Q}\in\mathrm{SO}(2),\,\boldsymbol{\nu}\in\mathbb{R}^2} \quad \|\boldsymbol{\nu}\|_2^2(\mathbf{1}_{n_1}^T\mathbf{\Pi}\mathbf{1}_{n_2}) + \sum_{i,j'}\|(\mathbf{s}_i - \mathbf{s}_{\mathrm{cm}}) - \mathbf{Q}(\mathbf{s}'_{j'} - \mathbf{s}'_{\mathrm{cm}})\|_2^2 \tag{53}$$

Where the independence of the left and right primal objectives yields that the minimizer is simply $\boldsymbol{\nu}^\star = \mathbf{0}$. After the optimization for the rotation, the optimal translation is simply: $\mathbf{h}^\star = -(\mathbf{Q}^\star)^T\mathbf{s}_{\mathrm{cm}} + \mathbf{s}'_{\mathrm{cm}}$. Thus, one may simply focus on the problem:

$$\min_{\mathbf{Q}\in\mathrm{SO}(2)} \quad \sum_{i,j'}\mathbf{\Pi}_{ij'}\|(\mathbf{s}_i - \mathbf{s}_{\mathrm{cm}}) - \mathbf{Q}(\mathbf{s}'_{j'} - \mathbf{s}'_{\mathrm{cm}})\|_2^2 \tag{54}$$

28

The presence of the joint distribution keeps this from being set in the standard form which Wahba's problem is presented and solved in. We give a simple equivalent form, introducing the center-shifted coordinate matrices across spatial locations in the slices:

$$\mathbf{S}_{\text{cm}}^{(1)} = \begin{pmatrix} \mathbf{s}_1 - \mathbf{s}_{\text{cm}} & \ldots & \mathbf{s}_{n_1} - \mathbf{s}_{\text{cm}} \end{pmatrix}$$

$$\mathbf{S}_{\text{cm}}^{(2)} = \begin{pmatrix} \mathbf{s}'_{1'} - \mathbf{s}'_{\text{cm}} & \ldots & \mathbf{s}'_{n'_2} - \mathbf{s}'_{\text{cm}} \end{pmatrix}$$

And consider the equivalent objective, with vec denoting the vectorization operation which column-stacks a matrix, $\mathbf{\Pi}^{1/2}$ denoting the element-wise square-root of the entries of $\mathbf{\Pi}$, and $\odot$ denoting the elementwise, or Hadamard, product:

$$\min_{\mathbf{Q} \in \text{SO}(2)} \left\| \left(\mathbf{1}_2 \, \text{vec} \left((\mathbf{\Pi}^{1/2})^T \right) \odot \left(\mathbf{S}_{\text{cm}}^{(1)} \otimes \mathbf{1}_{n_2}^T \right) \right) - \mathbf{Q} \left(\mathbf{1}_2 \, \text{vec} \left((\mathbf{\Pi}^{1/2})^T \right) \odot \left(\mathbf{1}_{n'}^T \otimes \mathbf{S}_{\text{cm}}^{(2)} \right) \right) \right\|_F^2 \tag{55}$$

We rename the matrices to be concise as $\mathbf{G}^{(1)}$, $\mathbf{G}^{(2)}$:

$$\min_{\mathbf{Q} \in \text{SO}(2)} \left\| \mathbf{G}^{(1)} - \mathbf{Q}\mathbf{G}^{(2)} \right\|_F^2 \tag{56}$$

The simple solution [10] can be given using an SVD of $\mathbf{G}^{(1)}(\mathbf{G}^{(2)})^T = \mathbf{U}\mathbf{\Sigma}\mathbf{V}^T$. Where the final orthogonal transformation would be given as $\mathbf{Q} = \mathbf{U}\mathbf{V}^T$. If one adds the restriction that $\det\left(\mathbf{U}\mathbf{V}^T\right) = 1$ for a rotation, one would find $\mathbf{Q}$ as:

$$\mathbf{Q} = \mathbf{U} \, \text{diag} \left(1 \quad \det\left(\mathbf{U}\mathbf{V}^T\right) \right) \mathbf{V}^T.$$

S7 Generate feature (expression) vectors for simulated data

S7.1 Generate feature vectors for simulated 1D slices

Our simplest experiment considers a pair of *one-dimensional* tissue slices with the same number of spots (51 total). Writing N in place of 25 for clarity, the spatial coordinates of the first and second slices are given by identical matrices, namely $\mathbf{S}^{(1)} \equiv \mathbf{S}^{(2)} = \begin{bmatrix} -N & -(N-1) & \ldots & -1 & 0 & 1 & \ldots & (N-1) & N \end{bmatrix}$, understood as a column vector. Synthetic features are constructed by first assigning one of two cell type labels ("A" or "B") to each spot, and then assigning numerical features based on cell type. As in 2.3.1, cell types partition each domain, we write these as $\mathcal{P}_1$ and $\mathcal{P}_2$, where:

$$\mathcal{P}_1(\text{A}) = \{-N, -N+1, \ldots w_1 - 1, w_1\}, \quad \mathcal{P}_1(\text{B}) = \{w_1 + 1, \ldots, N\}\}$$
$$\mathcal{P}_2(\text{A}) = \{-N, -N+1, \ldots w_2 - 1, w_2\}, \quad \mathcal{P}_2(\text{B}) = \{w_2 + 1, \ldots, N\},\}$$

setting $w_1 = -10$ and $w_2 = 5$ in the experiment to be the "pivots" marking a change in cell type.

We generate eight-dimensional feature by sampling random vectors $\boldsymbol{v}_1, \boldsymbol{v}_2, \boldsymbol{v}_3, \boldsymbol{v}_4$ independently and uniformly from the unit sphere of $\mathbb{R}^4$. Let $\mathbf{0} \in \mathbb{R}^4$ be the zero vector, and let $\circ$ denote concatenation of vectors. We set $\tilde{\boldsymbol{v}}_1 := \boldsymbol{v}_1 \circ \mathbf{0}$, $\tilde{\boldsymbol{v}}_2 := \boldsymbol{v}_2 \circ \mathbf{0}$, $\tilde{\boldsymbol{v}}_3 := \mathbf{0} \circ \boldsymbol{v}_3$ and $\tilde{\boldsymbol{v}}_4 := \mathbf{0} \circ \boldsymbol{v}_4$. Over cell type A, we generate features by linearly interpolating feature $\tilde{\boldsymbol{v}}_1$ at spot $-N$ with feature $\tilde{\boldsymbol{v}}_2$ at spot w_1 or w_2, depending on the slice. Over cell type B, we generate features by linearly interpolating feature $\tilde{\boldsymbol{v}}_3$ at either w_1 or w_2, with feature $\tilde{\boldsymbol{v}}_4$ at spot N. Thus, each cell type is characterized by a feature gradient in four dimensions, and the features at distinct cell types are orthogonal by design.

S7.2 Generate feature vectors for simulated 2D slices

We generalize the above by defining a two-dimensional model of tissue slices. Let E denote the centered, circular ellipse of radius $r = 25$:

$$E = \left\{ \mathbf{s} \equiv (x, y) \in \mathbb{R}^2 : \frac{x^2}{r^2} + \frac{y^2}{r^2} \leq 1 \right\}$$

Let $\mathbb{T}$ be the subset of the integer square lattice $\mathbb{Z}^2$ consisting of all integer pairs whose sum is odd: $\mathbb{T} = \{(x, y) \in \mathbb{Z}^2 : (x + y) \bmod 2 = 1\}$. Then $\mathbb{T}$ is a triangular lattice, mimicking the spatial organization of SRT data output by the Visium platform. Let $\mathbf{S}^{(1)} = \mathbf{S}^{(2)} = \mathbf{S}$ denote the stack of spatial coordinates associated to the set $E \cap \mathbb{T}$.

As above, we use a simple spatial condition to partition each slice into two pieces. Here, we set two "pivot" lines, given by $y = w_1$ and $y = w_2$. The cell type partitions $\mathcal{P}_1, \mathcal{P}_2$ over the two slices are defined as follows:

$$\mathcal{P}_1(A) = \{\mathbf{s} \equiv (x,y) \in E \cap \mathbb{T} : y > w_1\}, \quad \mathcal{P}_1(B) = \{\mathbf{s} \equiv (x,y) \in E \cap \mathbb{T} : y \le w_1\}$$
$$\mathcal{P}_2(A) = \{\mathbf{s} \equiv (x,y) \in E \cap \mathbb{T} : y > w_2\}, \quad \mathcal{P}_2(B) = \{\mathbf{s} \equiv (x,y) \in E \cap \mathbb{T} : y \le w_2\}$$

for $w_1, w_2 = \pm 10$.

We assign features in a similar manner to the one-dimensional case. Previously we assigned features to the boundary of cell type segments and linearly interpolated between these.

In this slightly more general setting, let $R_i(A)$ and $R_i(B)$ denote (smallest) bounding rectangles for sets $\mathcal{P}_i(A)$ and $\mathcal{P}_i(B)$ for slices $i = 1, 2$.

We assign the first four unit vectors in the standard basis $(\mathbf{e}_j)_{j=1}^8$ of $\mathbb{R}^8$ to cell type A, and the last four to cell type B. The top and bottom sides of $R_i(A)$ are assigned to features $\mathbf{e}_1$ and $\mathbf{e}_3$, while the left and right sides of the rectangle are assigned to features $\mathbf{e}_2$ and $\mathbf{e}_4$. We make similar assignments for $R_i(B)$ using the last four basis vectors. At each spot $\mathbf{s}$, lying in some bounding rectangle R for its cell type, the feature assigned to $\mathbf{s}$ is a convex combination of the features decorating the top and bottom sides of R, plus the features decorating the left and right sides of R. In particular, for $R = [x_{\min}, x_{\max}] \times [y_{\min}, y_{\max}]$ and $(x,y) \in R$, the coefficients λ_x, λ_y are defined as:

$$\lambda_x = \frac{x - x_{\min}}{x_{\max} - x_{\min}}, \qquad \lambda_y = \frac{y - y_{\min}}{y_{\max} - y_{\min}}$$

Thus, for a given cell type we have two gradients along the x and y direction which are scaled equivalently between the two slices $\mathbf{S}^{(1)}$ and $\mathbf{S}^{(2)}$ which we seek to align. The final feature vector within cell type A is therefore given as

$$\mathbf{f}_A(x,y) = \lambda_x \mathbf{f}_{x,L} + (1 - \lambda_x)\mathbf{f}_{x,R} + \lambda_y \mathbf{f}_{y,T} + (1 - \lambda_y)\mathbf{f}_{y,B}$$

and repeat this for cell type B as

$$\mathbf{g}_B(x,y) = \lambda_x \mathbf{g}_{x,L} + (1 - \lambda_x)\mathbf{g}_{x,R} + \lambda_y \mathbf{g}_{y,T} + (1 - \lambda_y)\mathbf{g}_{y,B}$$

choosing features which are mutually-orthogonal–for simplicity 8-dimensional unit vectors $\mathbf{e}_{1:8}$. Between $\mathbf{S}^{(1)}$ and $\mathbf{S}^{(2)}$ these features are consistent, and $\lambda_x, \lambda_y \in [0,1]$ gives the proportion of each feature depending on how far the (x,y) coordinate is along the axis of each ellipse within a given cell type. I.e. for $(x_1, y_1) \in \mathbf{S}^{(1)}$, $(x_2, y_2) \in \mathbf{S}^{(2)}$ we have that if $\lambda_{x_1}^A = \lambda_{x_2}^A$ and $\lambda_{y_1}^A = \lambda_{y_2}^A$ then $\mathbf{f}_A(x_1, y_1) = \mathbf{f}_A(x_2, y_2)$ and the two features should be aligned between timepoints 1 and 2 (likewise for cell type B). As the features are chosen to be orthogonal, this alignment is unique. To model noise, we assume that the data we observe at each point (x,y) is distributed as $\sim \mathcal{N}(\mathbf{f}_A(x,y), \sigma^2 \mathbb{1}_8)$ for cell type A and $\sim \mathcal{N}(\mathbf{g}_B(x,y), \sigma^2 \mathbb{1}_8)$ for cell type B for varying levels of σ.

S8 Benchmarking methods

PASTE [45] By design, PASTE cannot align spatiotemporal data and does not infer cell growth and death because it uses balanced OT. For the purpose of benchmarking experiments in this work, we relax PASTE's balanced constraints so that we optimize the unbalanced version of the PASTE objective. For the alignment matrix $\mathbf{\Pi}$ computed by relaxed PASTE, we then take the difference between the row sums of $\mathbf{\Pi}$ and the uniform distribution $\mathbf{g}_1$ (Eq. (4)) as PASTE's inferred growth $\boldsymbol{\xi}$.

moscot [21] We use `moscot.problems.spatiotemporal.SpatioTemporalProblem` for solving spatiotemporal alignment problems in this work using moscot. For the alignment matrix $\mathbf{\Pi}$ computed by moscot, we take the difference between the row sums of $\mathbf{\Pi}$ and the uniform distribution $\mathbf{g}_1$ as moscot's inferred growth $\boldsymbol{\xi}$. For benchmarking experiments related to growth *rates* instead of growth (§**??**), we use the numbers returned by `SpatioTemporalProblem.posterior_growth_rates` as moscot's inferred growth *rates* over spots in timepoint t_1.

SLAT [44] We use `scSLAT.model.run_SLAT` of the scSLAT package for computing an embedding for each spot in each timepoint. We then use `scSLAT.model.spatial_match` to compute an alignment between spots across the two timpoints. We construct a matrix $\mathbf{\Pi}$ such that $\mathbf{\Pi}_{ij'} = 1$ if spot i in timepoint 1 is the best spot aligned to spot j' in timepoint 2. We then divide $\mathbf{\Pi}$ by the number of spots at timpoint 1 to convert it into a semi-relaxed transport matrix. We take the difference between the row sums of $\mathbf{\Pi}$ and the uniform distribution $\mathbf{g}_1$ as SLAT's inferred growth $\boldsymbol{\xi}$.
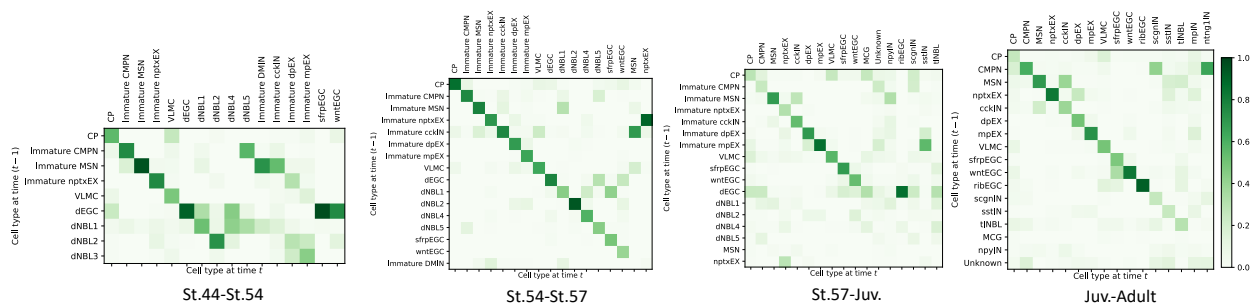
Figure S1: Cell type transition matrix at each pair of timepoints during axolotl brain development Rows are cell types at the previous timepoint. Columns are cell types at the next timepoint. Matrices are column normalized.

STalign [8] We first "rasterize" the spatial positions of our input data into two greyscale images. This effectively convolves a scatterplot of the spatial data with two-dimensional Gaussian noise, to produce an image approximating each tissue slice. We then ran STalign's `LDDMM` on the pair of images, outputting a diffeomorphism φ (which maps the first slice to the second) and its inverse φ^{-1} (mapping the second slice to the first). We then use φ^{-1} to construct a transport plan Π as follows: for spot j' in the second slice, we apply φ^{-1} to $s_{j'}$, and select s_i in the first slice which is closest to $\varphi^{-1}(s_{j'})$. Then we set $\Pi_{ij'} = 1$, and repeat this procedure for each spot in the second slice, filling out each column of Π. The transport plan is thus a deterministic map from the spots of the second slice into those of the first. We then divide Π by the number of spots at timpoint 1 to convert it into a semi-relaxed transport matrix. We take the difference between the row sums of Π and the uniform distribution g_1 as STalign's inferred growth ξ.